

CHAPTER 2

LITERATURE REVIEW

2.1 Introduction

Among the 32 crystallographic point groups describing all crystalline systems, 11 are centrosymmetric and contain an inversion center. In that case polar properties become not possible because any polar vector may be inverted by an existing symmetry transformation. All other 21 point groups without an inversion center (except the point group 432) can exhibit piezoelectricity which describes the coupling between mechanical and electrical energies in a material. An external mechanical stress X leads to a change in the electric polarization P or dielectric displacement D respectively or an external electric field E causes an elastic strain x . The relation is given by the piezoelectric coefficient d_{ijk} being a third rank tensor:

$$D_i = d_{ijk}X_{jk} \quad X_{ij} = d_{ijk}E_k \quad (2.1)$$

There are 10 polar groups with a unique polar axis among the 21 point groups without an inversion center. This class of crystals may show a spontaneous polarization parallel to the polar axis.

Following Maxwell's equations, the spontaneous polarization is connected with surface charges $P_s = \sigma$. The surface charges in general are compensated by charged defects. A temperature change changes the spontaneous polarization. This effect is called the pyroelectric effect [25].

If it is possible to reorient the spontaneous polarization of a material between crystallographically equivalent configurations by an external electric field, then in analogy to ferromagnetic one speaks about ferroelectrics. Thus, it is not the existence of spontaneous polarization alone, but the “switchability” by an external field which defines a ferroelectric material. Figure 2.1 displays a characteristic hysteresis loop occurring during the reversal of the polarization in a ferroelectric [25].

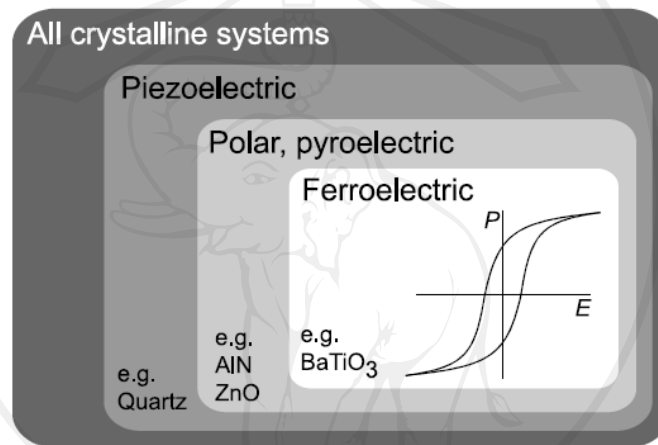


Figure 2.1 Classification of the crystallographic groups by their electrical properties [25]

2.2 Dielectric polarization

2.2.1 Macroscopic and microscopic views

In accordance to the Poisson equation, the source of the dielectric displacement \vec{D} is given by the density of free (conducting) charges ρ :

$$\text{div} \vec{D} = \rho_{\text{free}} \quad (2.2)$$

The overall charge neutrality of matter in an external field is described by:

$$\vec{D} = \epsilon_0 \vec{E} + \vec{P} \quad (2.3)$$

The vacuum contribution caused by the externally applied electric field is represented by the term $\epsilon_0 \vec{E}$, and the electrical polarization of the matter in the system is described by \vec{P} , e.g. [26]. This relation is independent of the nature of the polarization which could be pyroelectric polarization, by piezoelectric polarization or dielectric polarization (by an external electric field).

Considering a simple parallel plate capacitor filled with matter (see Figure 2.2), two cases have to be distinguished: (i) If the applied voltage is kept constant ($E = \text{const}$, short circuit condition), additional free charges need to flow into the system to increase D according to Equation (2.2). If the charges on the plates are kept constant ($D = \text{const}$, open circuit condition), the electric field E and, hence, the voltage between the plates will decrease according to Equation (2.3).

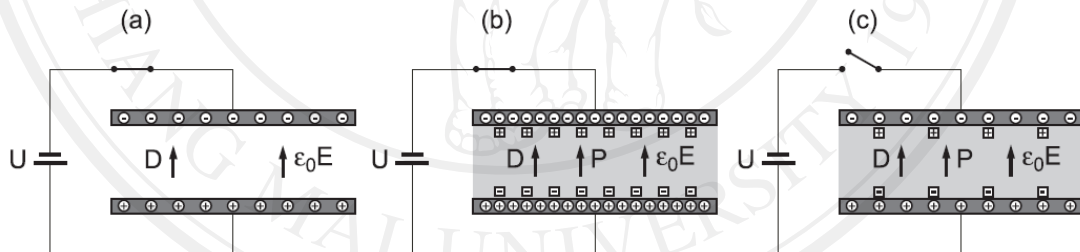


Figure 2.2 Parallel plate capacitor (a) without any dielectric, (b) filled with dielectric under short circuit condition ($E = \text{constant}$) and (c) filled with dielectric under open circuit condition ($D = \text{constant}$) [25]

For a pure dielectric response of the matter the polarization is proportional to the electric field in a linear approximation by

$$P = \epsilon_0 \chi_e E \quad \text{or} \quad D = \epsilon_0 \epsilon_r E \quad (2.4)$$

The dielectric susceptibility χ is related to the relative dielectric constant ϵ_r by $\chi = \epsilon_r - 1$. Equations (2.4) are only valid for small fields. Large amplitudes of the ac field lead to strong non-linearities in dielectrics, and to sub-loops of the hysteresis in ferroelectrics. Furthermore, the dielectric response depends on the bias fields as shown in Figure 2.3. From the device point of view this effect achieves the potential of a tunable dielectric behavior, e. g. for varactors.

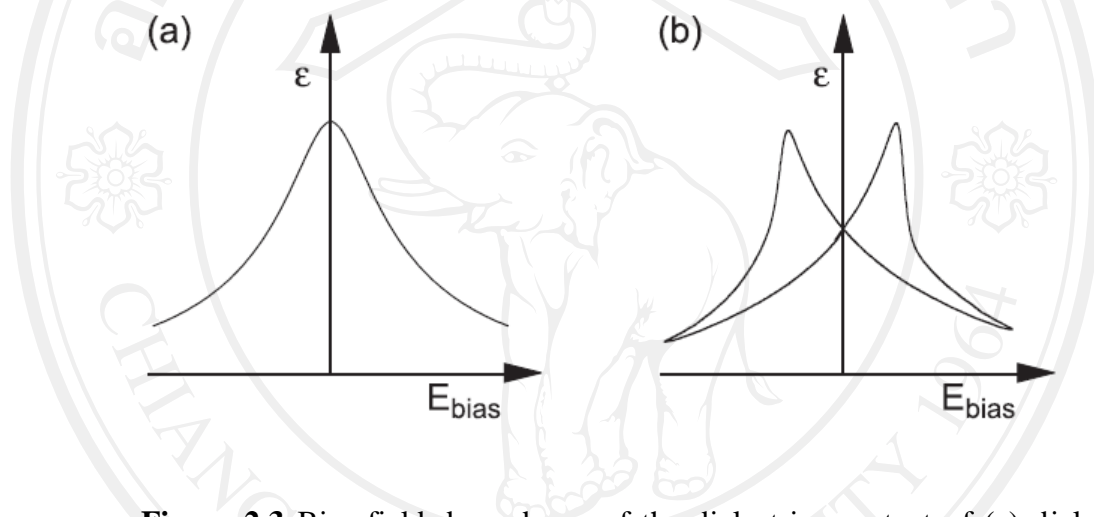


Figure 2.3 Bias field dependence of the dielectric constant of (a) dielectric and (b) ferroelectric materials [25]

Equations (2.3) and (2.4) describe the mean properties of the dielectric. This macroscopic point of view does not consider the microscopic origin of the polarization [27]. The macroscopic polarization P is the sum of all the individual dipole moments p_j of the material with the density N_j .

$$P = \sum_j N_j p_j \quad (2.5)$$

In order to find a correlation between the macroscopic polarization and the microscopic properties of the material a single (polarizable) particle is considered. A

dipole moment is induced by the electric field at the position of the particle which is called the local electric field E_{loc}

$$p = \alpha E_{loc} \quad (2.6)$$

where α is the polarizability of an atomic dipole. If there is no interaction between the polarized particles, the local electric field is identical to the externally applied electric field $E_{loc} = E_0$, resulting in a simple relation between the susceptibility and the polarizability $\epsilon_0\chi = N_j\alpha_j$.

In condensed matters, the density and therefore the electrostatic interaction between the microscopic dipoles is quite high. Hence, the local field E_{loc} at the position of a particular dipole is given by the superposition of the applied macroscopic field E_0 and the sum of all other dipole fields. For cubic structures and for induced dipoles (ionic and electronic polarization), the calculation reveals a relation between the atomic polarizability α and the macroscopic permittivity $\epsilon = \epsilon_0\epsilon_r$, which is referred to the Clausius-Mossotti equation [28].

$$\epsilon = \frac{\epsilon_0 + 2N_j\alpha_j}{\epsilon_0 - N_j\alpha_j} \quad (2.7)$$

2.2.2 Mechanisms of polarization

In general, there are five different mechanisms of polarization which can contribute to the dielectric response [27].

- **Electronic polarization** exists in all dielectrics. It is based on the displacement of the negatively charged electron shell against the positively charged core. The electronic polarizability α_{el} is approximately proportional to the volume of the electron

shell. Thus, in general α_{el} is temperature-independent, and large atoms have a large electronic polarizability.

- **Ionic polarization** is observed in ionic crystals and describes the displacement of the positive and negative sub-lattices under an applied electric field.
- **Orientation polarization** describes the alignment of permanent dipoles. At ambient temperatures, usually all dipole moments have statistical distribution of their directions. An electric field generates a preferred direction for the dipoles, while the thermal movement of the atoms perturbs the alignment. The average degree of orientation is given by the Langevin function $\langle \alpha_{or} \rangle = p^2/(3k_B T)$ where k_B denotes the Boltzmann constant and T the absolute temperature.
- **Space charge polarization** could exist in dielectric materials which show spatial inhomogeneities of charge carrier densities. Space charge polarization effects are not only of importance in semiconductor field-effect devices, they also occur in ceramics with electrically conducting grains and insulating grain boundaries (so-called Maxwell-Wagner polarization).
- **Domain wall polarization** plays a decisive role in ferroelectric materials and contributes to the overall dielectric response. The motion of a domain wall that separates regions of different oriented polarization takes place by the fact that favored oriented domains with respect to the applied field tends to grow.

The total polarization of dielectric material results from all the contributions discussed above. The contributions from the lattice are called intrinsic contributions, in contrast to extrinsic contributions.

$$\epsilon = \epsilon_{elec} + \epsilon_{ion} + \epsilon_{or} + \epsilon_{dw} + \epsilon_{sc} \quad (2.8)$$

which ϵ_{elec} and ϵ_{ion} are intrinsic while ϵ_{or} , ϵ_{dw} and ϵ_{sc} are extrinsic.

Each contribution stems from a short-range movement of charges that responds to an electric field on different time scales and, hence, through a Fourier transform, in different frequency regimes. If the oscillating masses experience a restoring force, a relaxation behavior is found (for orientation, domain walls, and space charge polarization). Resonance effects are observed for the ionic and electronic polarization. The dispersion of the dielectric function is shown in Figure 2.4, and holds the potential to separate the different dielectric contributions.

The space charge polarization is caused by a drift of mobile ions or electrons which are confined to outer or inner interfaces. Depending on the local conductivity, the space charge polarization may occur over a wide frequency range from mHz up to MHz. The polarization due to the orientation of electric dipoles takes place in the frequency regime from mHz in the case of the reorientation of polar ligands of polymers up to a few GHz in liquids such as water. It is often possible to distinguish between space charge and orientation because of the temperature dependence of α_{or} . In the infrared region between 1 and 10 THz, resonances of the molecular vibrations and ionic lattices constituting the upper frequency limit of the ionic polarization are observed. The resonance of the electronic polarization is around 10^{15} Hz. It can be investigated by optical methods.

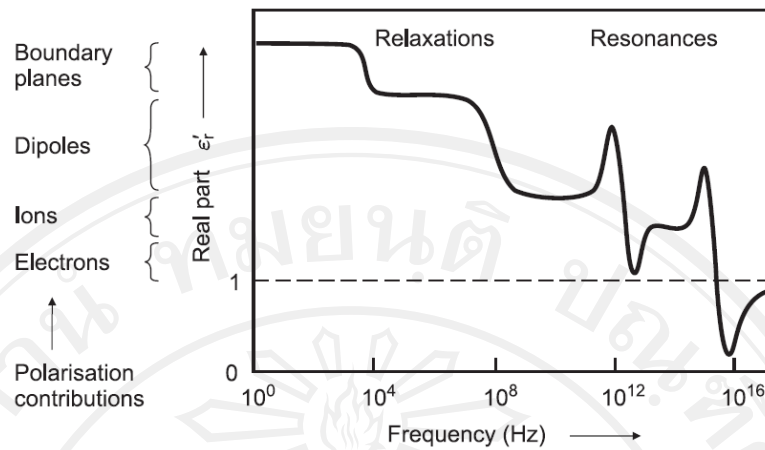


Figure 2.4 Frequency dependence of real part of the dielectric function [25]

The dispersion of the dielectric response of each contribution leads to dielectric losses of the matter which can be mathematically expressed by a complex dielectric permittivity:

$$\epsilon = \epsilon' + i\epsilon'' \quad (2.9)$$

Dielectric losses are usually described by the loss tangent:

$$\tan\delta = \frac{\epsilon''}{\epsilon'} \quad (2.10)$$

It should be taken into account that the general definition of the $\tan \delta$ is related to the ratio of loss energy and reactive energy (per period), i. e. all measurements of the loss tangent also include possible contributions of conductivity σ of a non-ideal dielectric given by $\tan \delta = \sigma/\omega\epsilon'$.

2.3 Normal ferroelectrics

The relation between the net macroscopic polarization of a ferroelectric crystal and the externally applied electric field is given by a hysteresis loop. When an electric field is applied to a ferroelectric, these dipoles can be reoriented with respect to the

direction of the applied field. The major difference between ferromagnetic and ferroelectric is the fact that the polarization of the magnetic dipoles in ferromagnetics is attributed to the magnetic dipoles in each individual atom; in ferroelectrics, the polarization is due to the crystal structure as a whole and not of the individual atoms.

As a crystal polarizes, a domain structure is formed. The domain will initially nucleate randomly with their polarization vectors along one of the allowed directions. In order to change the polarization direction, ferroelectric domain walls must be shifted. The driving force for this movement is free energy for the electronic dipole orientation. In ferroelectrics, the dipoles align with the applied electric field and assume a lower energy state compared to that for the spontaneously polarized direction. The energy required to reorient the domains can be seen in the area of the electric displacement versus applied field hysteresis loop, as seen in Figure 2.5 [29].

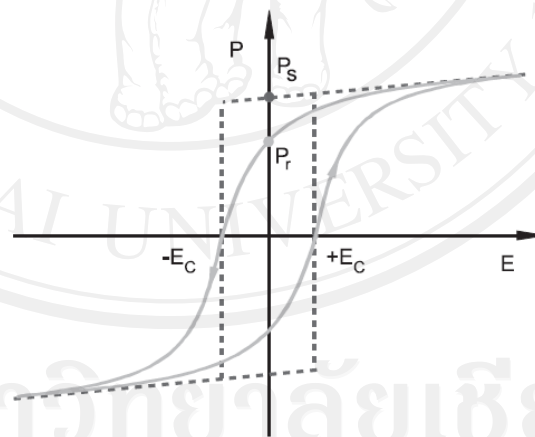


Figure 2.5 A typical ferroelectric hysteresis loop of single crystal (dashed line) and polycrystal sample (full line) [25]

The temperature at which the crystal structure transforms from the paraelectric state into the ferroelectric state is called the Curie point [30]. According to the Curie-Weiss law, the dielectric constant obeys the equation:

$$\frac{1}{\epsilon} = \frac{(T - T_0)}{C} \quad (2.11)$$

where, C is the Curie-Weiss constant, T is the temperature and, T_0 is the Curie-Weiss temperature that is less than T_C . The Curie point is the actual transformation temperature, while the Curie-Weiss temperature is found by extrapolating the plot of the Curie-Weiss law, as shown in Figure 2.6 [31]. The Curie-Weiss temperature can be as much as ten degrees lower than the Curie point for first-order phase transitions and the two are equal for a second order phase transition. First-order phase transitions are those in which the first derivative of the free energy expansion with respect to temperature is discontinuous as shown in Figure 2.6(b). In second-order phase transitions, the second derivation is continuous as shown in Figure 2.6(a).

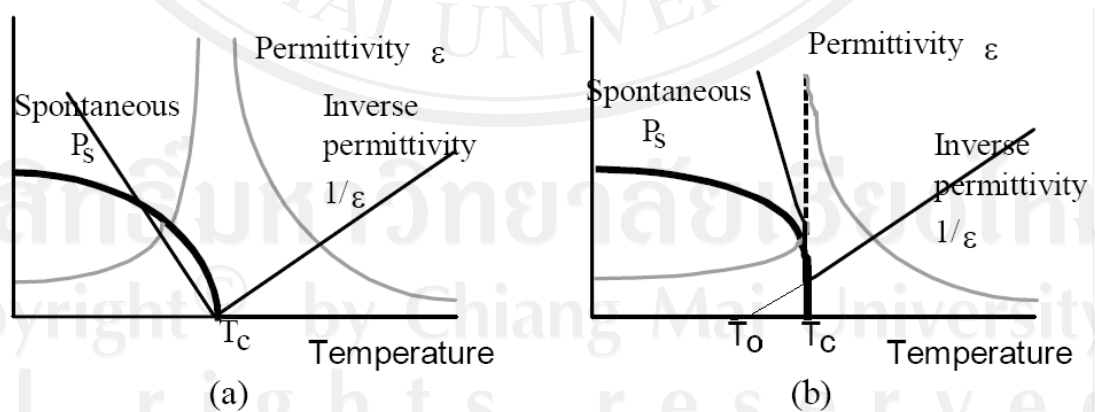


Figure 2.6 A general depiction of the temperature dependences of the spontaneous polarization, the dielectric constant, and the inverse dielectric constant

for a ferroelectric (a) second-order phase transitions and (b) first-order phase transitions [31]

2.4 Ferroelectric domains

When a ferroelectric single crystal is cooled below the phase transition temperature the electrical stray field energy caused by the non-compensated polarization charges is reduced by the formation of ferroelectric domains, see Figure 2.7. The configuration of the domains follows a head-to-tail condition in order to avoid discontinuities in the polarization at the domain boundary, $\nabla \cdot \vec{P} = \sigma$. The built-up of domain walls, elastical stress fields as well as free charge carriers counteract the process of domain formation. In addition, an influence of vacancies, dislocations and dopants exists.

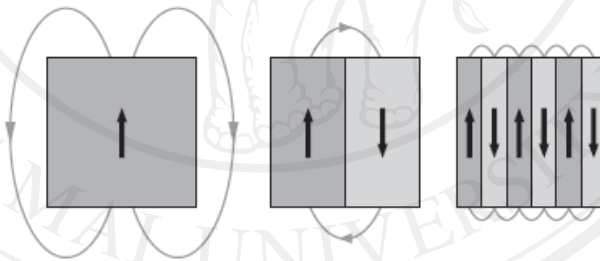


Figure 2.7 Reduction of electrical stray field energy by domain formation [25]

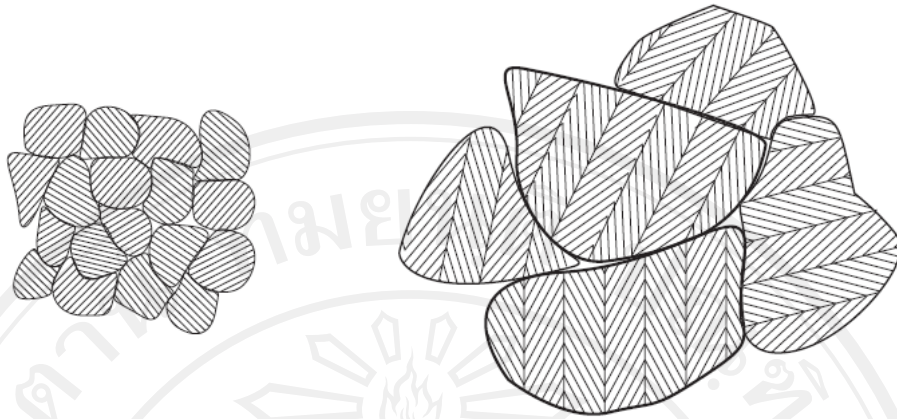


Figure 2.8 Scheme of domain pattern of fine grained BaTiO₃ ceramic (left) and coarse grained BaTiO₃ ceramic (right) [25]

In polycrystalline bulk ceramics the pattern of domains is quite different because the domain structure of each grain is formed under elastic clamped conditions by its surrounding neighbors, whereas a single crystal is free [32]. It should be noted that only non-180° domains, i.e. 90° domains (for tetragonal structures) or 71° and 109° domains (for rhombohedral structures), have the potential to reduce elastic energy. There exists two types in coarse grained BaTiO₃, called herringbone and square net pattern. The first one is by far the most common in unpoled ceramics. As shown in Figure 2.8, by decreasing the grain size the domain pattern changes from a banded to a laminar structure [33].

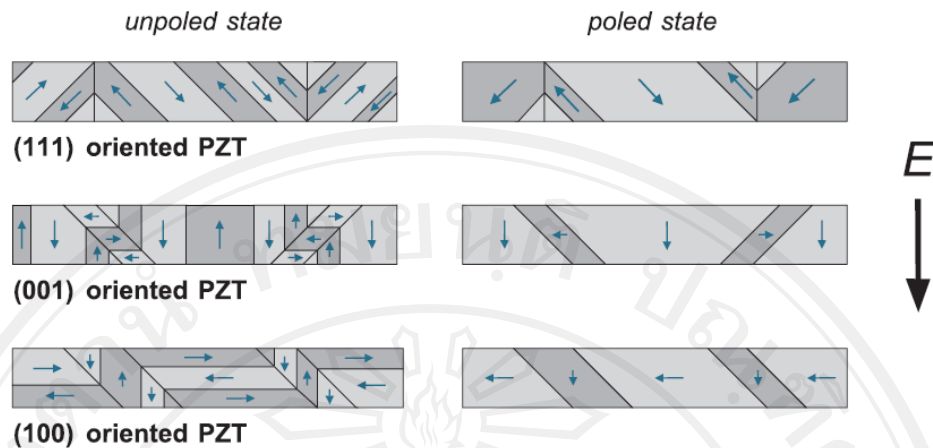


Figure 2.9 Domain structures of tetragonal PZT with different orientations [25]

Real ferroelectric thin films show polydomain patterns. In Figure 2.9 possible domain configurations of different textures of tetragonal films of $\text{PbZr}_{1-x}\text{Ti}_x\text{O}_3$ with $x > 0.48$ are depicted. For compressive stress the polarization is predominantly out-of-plane, (001), oriented. 90° as well as 180° -domains are expected. Such orientation could be realized by deposition of tetragonal PZT on magnesium oxide substrates [34]. Under the influence of an electric field the number of 180° -domains is decreased. The resulting pattern predominantly consists in 90° domains. A (100)-orientation, i. e. in-plane orientation of the polarization, is caused by tensile stress and is achieved by using a buffer layer of yttrium stabilized zirconium and an oxide electrode of lanthanum strontium cobaltate or by depositing on a (100)- SrTiO_3 -substrate with SrRuO_3 electrode [35]. The change of the domain structure by poling is similar to the (001)-orientation but, the a-axis orientation is still preferred. In standard systems for ferroelectric thin films, e.g. PZT with platinum electrodes on oxidized silicon wafers, the orientation of the crystallographic axes of PZT is in (111)-direction. Poling should evoke the single domain state while the “head-to-tail”

configuration is required. However, there are a lot of indications that non-180° domain walls are generally immobile. It could be shown that these ferroelastic domain walls become able to move, when the 2-D clamping of the film on the substrate is annulled by patterning the ferroelectric film into discrete islands using a focused ion beam [36].

2.4.1 The dynamics of domain wall motions in ceramics

If the domain walls are fixed and no other defects contribute to piezoelectricity in ceramics, then an averaging calculation would predict all the main intrinsic electromechanical properties when using appropriate values of single domain crystals and a simple orientation distribution. This calculation [37] has to take into account the dielectric, piezoelectric, and elastic interactions between the domains, their shape and configuration, and their degree of orientation. Muratake [38] first introduced a method that takes into account some interaction effects by considering electric and elastic boundary conditions of the grain. Turik [39] improved the Muratake model by using a laminar grain consisting of a stack of 90° or 180° domains. For the laminar grain of BT, the effective piezoelectric, elastic, and dielectric coefficients were calculated considering the boundary conditions between the domains. The experimentally determined piezoelectric constants d_{31} and d_{33} of BT ceramics are, however, much larger than the calculated ones. This deviation between calculated and measured piezoelectric constants had led Turik to suppose additional “orientational” contributions that may be caused by domain wall motions [40].

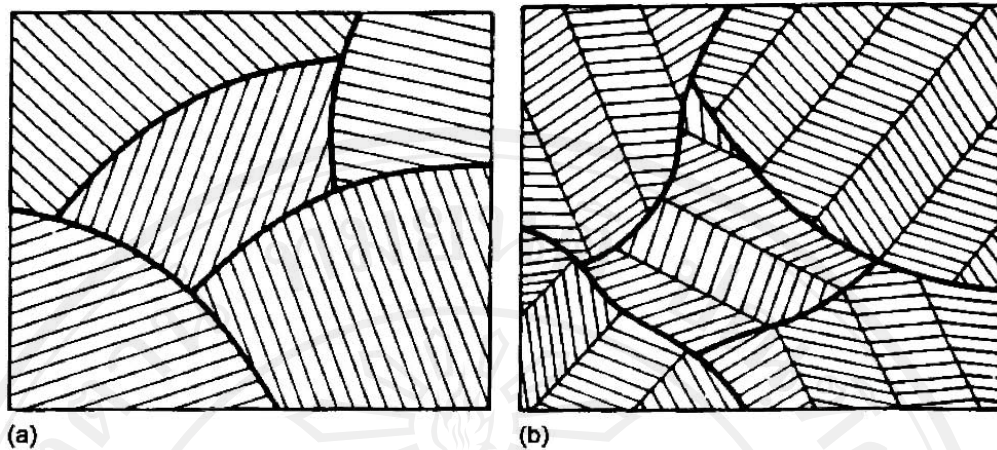


Figure 2.10 Domain structures in polycrystalline materials: (a) simple lamellar twinning. (b) banded twin structure in ceramics [41]

Since the 1980s, Arlt *et al.* (e.g., [41] and [42]) have systematically studied microstructure and dynamics of 90° domain wall motion in BT and PZT ceramics. They could explain the strong increase in the piezoelectric and dielectric coefficients by shifts and oscillations of 90° -type domain walls (90° in the tetragonal, 71° and 109° in the rhombohedral phase). They used Fousek's model [43] to evaluate the dielectric, piezoelectric, and elastic coefficients referring to a special distribution function and by averaging the domain contributions in every grain of the ceramic samples. A similar work was done by some Russian scientists (e.g., [44]). They considered some special distributions of domain structures in ceramics (the laminar twin structure) to assess the physical properties of ferroelectric ceramics.

All these models describe the average dynamic behavior of the domain wall motion in the single crystal with respect to the different orientations of polarizations. All these averaging methods have drawbacks and are of limited value for the calculation of the volume part of contributions to piezoelectric constants of ceramics.

The experimentally determined piezoelectric constants d_{31} and d_{33} are effectively larger than those calculated by the averaging methods. A similar disagreement was found for the dielectric constants, which in ceramics are much larger than expected from theoretical calculations.

2.4.2 Reversible and irreversible polarization contributions

To characterize ferroelectric materials usually the dependence of the polarization on the applied voltage is measured by means of a Sawyer-Tower circuit or by recording the current response to a voltage step. The $P(V)$ -hysteresis curve is used to determine the remanent polarization and coercive voltage, respectively coercive field. These two parameters are of critical importance to the design of external circuits of FeRAMs.

The ferroelectric hysteresis originates from the existence of irreversible polarization processes by polarization reversals of a single ferroelectric lattice cell. However, the exact interplay between this fundamental process, domain walls, defects and the overall appearance of the ferroelectric hysteresis is still not precisely known. The separation of the total polarization into reversible and irreversible contributions might facilitate the understanding of ferroelectric polarization mechanisms. Especially, the irreversible processes would be important for ferroelectric memory devices, since the reversible processes cannot be used to store information.

For ferroelectrics, mainly two possible mechanisms for irreversible processes exist. First, lattice defects which interact with a domain wall and hinder it from returning into its initial position after removing the electric field that initiated the domain wall motion (“pinning”) [45]. Second, the nucleation and growth of new domains which do not disappear after the field is removed again. In ferroelectric

materials the matter is further complicated by defect dipoles and free charges that also contribute to the measured polarization and can also interact with domain walls [46]. Reversible contributions in ferroelectrics are due to ionic and electronic very fast. The reorientation of dipoles and/or defect or free charges also contributes to the total polarization. These mechanisms are usually much slower, but they also might be reversible (relaxation).

A domain wall under an external electric field moves in a statistical potential generated by their interaction with the lattice, point defects, dislocations, and neighboring walls. Reversible movement of the wall is regarded as a small displacement around a local minimum. When the driven field is high enough, irreversible jumps above the potential barrier into a neighboring local minimum occur (see Figure 2.11).

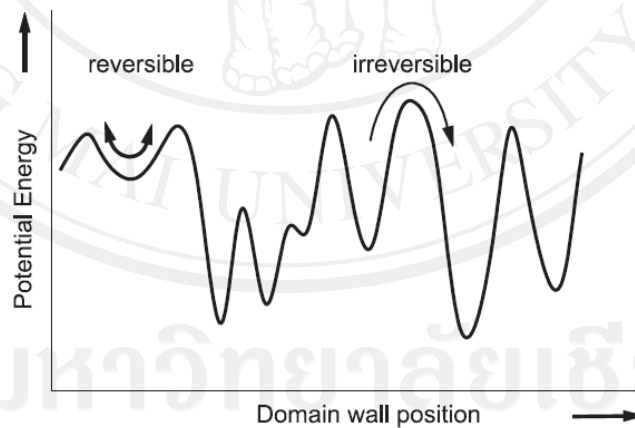


Figure 2.11 Movement of a domain wall in the lattice potential [25]

Based on these assumptions the measurement of the large signal ferroelectric hysteresis with additional measurements of the small signal capacitance at different bias voltages are interpreted in terms of reversible and irreversible parts of the

polarization. As shown for ferroelectric thin films in Figure 2.12, the separation is done by subtracting from the total polarization the reversible part, i. e. the integrated $C(V)$ -curve [47].

$$P_{irr}(V) = P_{tot}(V) - \frac{1}{A} \int_0^V C(V') dV' \quad (2.12)$$

Analogous $C(V)$ curves were recorded on PZT bulk ceramics with compositions around the morphotropic phase boundary (MPB). Figure 2.13 displays the relative permittivity as a function of DC-bias for a tetragonal ($x = 0.48$), a morphotropic ($x = 0.52$) and a rhombohedral ($x = 0.58$) sample. In contrast to thin films additional “humps” observed in the $\varepsilon(E)$ curves. This could be explained by different coercive fields for 180° and non- 180° domains [48]. Their absence in ferroelectric thin films could be taken as evidence for suppressed non- 180° domain switching in thin films [49].

A further approach to separate the reversible and irreversible 90° and non- 90° contributions is the investigation of the piezoelectric small and large signal response of the ferroelectric material. While both 180° and non- 180° walls contribute to the permittivity, only non- 180° walls affect the piezoelectric properties. A displacement of a 180° wall does not change the strains and thus yields no piezoelectric response.

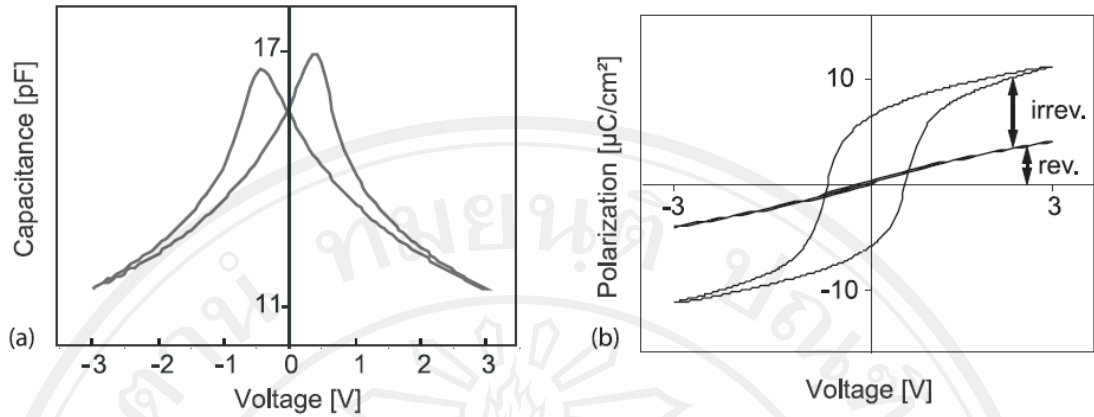


Figure 2.12 (a) $C(V)$ - curve and (b) reversible and irreversible contribution to the polarization of a ferroelectric SBT thin film [25]

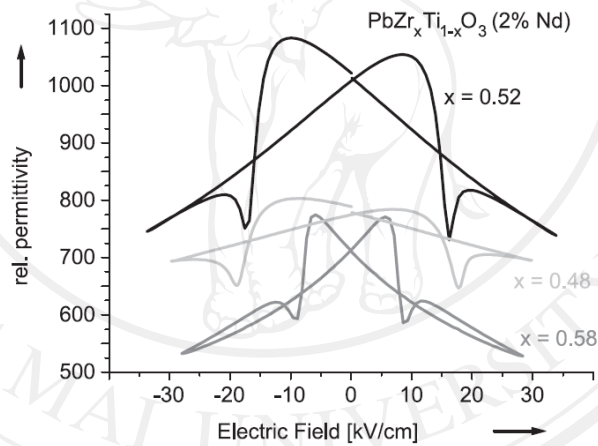


Figure 2.13 Relative permittivity of 2% Nd-doped $\text{Pb}(\text{Zr}_x\text{Ti}_{1-x})\text{O}_3$ bulk ceramics [25].

Analogue to the dielectric case, the reversible contribution to the strain can be determined by the integration of the piezoelectric small signal coefficient d_{3j} over the applied bias field.

$$\chi_{3j,rev}(E_{bias}) = \int_0^{E_{bias}} d_{3j}(E'_3) dE'_3 \quad (2.13)$$

Figure 2.14 displays the results of the d_{33} coefficient as function of the bias field, the large signal x_{33} response (“butterfly loop”) as well as constructed $x_{33,rev}$ curve of the same PZT thin film. The curves were taken by double-beam laser interferometry having a resolution better than 1 μm [50]. In contrast to bulk ceramics almost the complete strain response of the film appeared to originate from reversible processes. Since the polarization response of the film was determined by both 180° and non- 180° domain wall motion and the piezoelectric response was solely due to non- 180° boundaries, the presented results are evidence that most reversible domain wall motions in ferroelectric thin films are due to reversible motion of non- 180° domain walls. The clamping effect of the substrate which entails rather stringent mechanical boundary conditions apparently only allows for minute motions of the non- 180° walls, which immediately return to their initial positions when the external electric field that initiated the motion is returned to zero.

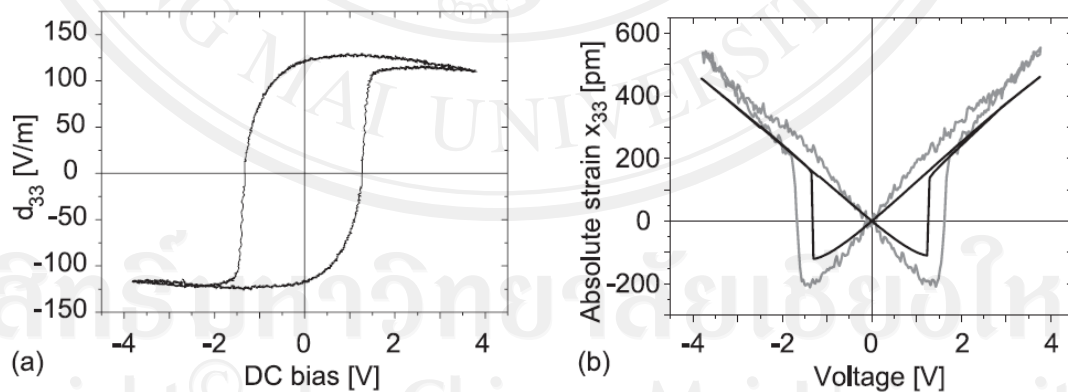


Figure 2.14 (a) Piezoelectric coefficient d_{33} and (b) “Butterfly” loop and integrated d_{33} response of a PZT 45/55 film [25]

2.4.3 Ferroelectric switching

The polarization reversal in single crystals has been intensively investigated by direct observation of the formation and the movement of the domain walls. E.g., in BaTiO₃ single crystals it was found by Merz [51], and Fousek [52] that in response to a voltage step the process happens by forming of opposing 180° or orthogonal 90° domains in the shape of needles and wedges. Both, the resulting maximum displacement current i_{max} as well as the switching time t_s , which is the most significant quantity and describes the duration of the polarization reversal, were measured as a function of the applied field E and follow empirical laws

$$i_{max} = i_0 \cdot \exp(-\alpha/E), \quad (2.14)$$

$$t_s = t_0 \cdot \exp(\alpha/E), \quad (2.15)$$

where i_0 and t_0 are a constants. The constant activation field α in both equations is the same [53].

The above mentioned equations are only applicable when the applied field E is constant during the polarization reversal, i.e., the time constant of the dielectric charging τ_{RC} must be much smaller than the switching time t_s . The dielectric charging is determined by the capacitance of the sample and inevitable series resistors (source, lines etc.). The switching time is determined by many factors, the domain structure, the nucleation rate of opposite domains, the mobility of the domain walls, and many others.

2.5 Ferroelectric characterization

2.5.1 Hysteresis loop and characteristic values

Typical result of the measurement is the hysteresis curve of the polarization. In the following the nomenclature of characteristic values for the evaluation of the measured data is introduced ([54], see also Figure 2.15):

P_{r+} positive state of **remanent polarization** of the dynamically measured hysteresis loop

P_{rrel+} positive state of **relaxed remanent polarization**, relaxed for one second in the P_{r+} state. Equal to the positive state of remanent polarization of the quasi statically measured loop

P_{max+} state of polarization when the stimulating signal reaches its maximum value – **positive saturation**

V_{c+} positive **coercive voltage**, voltage where the polarization crosses the x -axis by increasing voltage values

P_{r-} , P_{rrel-} , P_{max-} , V_{c-} are the corresponding values for the negative field and polarization direction

P_s ($P_{max+} - P_{rrel-}$) change of polarization when the sample is switched from the negative state of the relaxed remanent polarization into the positive saturation - **switching case**

P_{ns} ($P_{max+} - P_{rrel+}$) change of polarization when the sample is driven into the positive saturation from the positive state of the relaxed remanent polarization – **nonswitching case**

ΔP_s ($P_s - P_{ns}$) detectable polarization difference between switching and non-switching case.

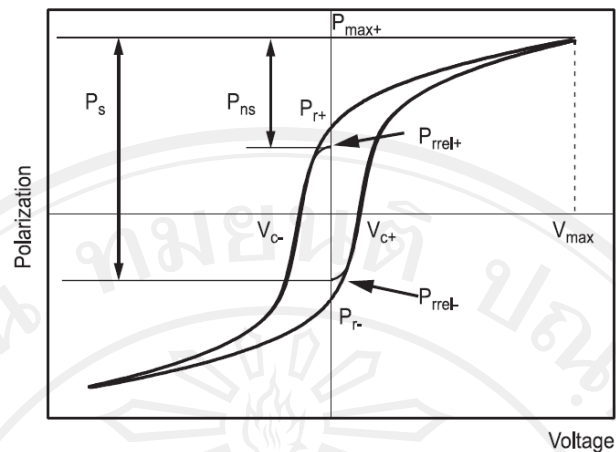


Figure 2.15 Nomenclature used [25]

2.5.2 Sawyer-Tower method

The Sawyer-Tower measurement circuit is based on a charge measurement method which relies on a reference capacitor in series with the ferroelectric capacitor [55]. The voltage drop across the reference capacitor is proportional to the polarization charge as defined by $V = Q/C$. But if the voltage on the reference capacitor increases, the voltage across the sample decreases (back voltage effect). So the reference capacitor is chosen much larger than the measured capacitor, e.g. if the reference capacitor is 100 times larger, the voltage drop is about 1%. This means the reference capacitor has to be adapted to each sample. The Sawyer-Tower method can be used up to high speed which is primarily limited by cable reflections. As parasitic effects, cabling capacitances of the wiring between sample, reference capacitor, and the recording amplifier are in parallel to the reference capacitor. Typical cable capacitance values are between 33 pF and 100 pF per meter. For small capacitors, the total measured capacitance is increased over the capacitance of the ferroelectric material. Furthermore, it is difficult to get precise reference capacitors which typically

have several percent tolerance, and additionally the cable capacitance adds to this capacitance. Furthermore the input resistance of the voltage measurement device is in parallel to the reference capacitor and discharges it with a corresponding time constant, therefore the Sawyer-Tower is less suitable for slow measurements.

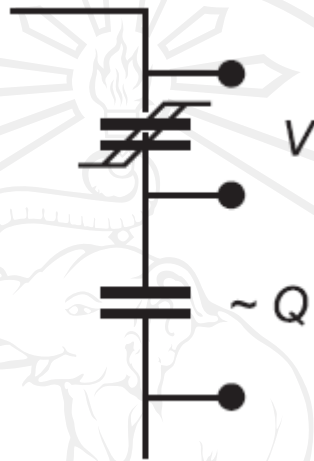


Figure 2.16 Schematic of a Sawyer-Tower hysteresis measurement method [25]

2.6 Power-law scaling relation

Consider a cooperatively interacting many-body system, such as a magnet, driven by an oscillating external perturbation, such as an oscillating magnetic field. The thermodynamic response of the system, e.g., the magnetization, will then also oscillate with necessary modifications in its form, and will lag behind the applied field due to the relaxational delay. This delay in the dynamic response gives rise to a nonvanishing area of the magnetization-field loop, a phenomenon we term dynamic hysteresis. When the time period of oscillation of the external perturbation becomes much less than the typical relaxation time of the thermodynamic system, the hysteresis loop becomes asymmetric around the origin and an interesting

thermodynamic phase arises spontaneously out of dynamically broken symmetries due to the competing time scales in such nonequilibrium driven systems [56].

In the example of a magnetic system, the time (t) variation of the magnetization $m(t)$ lags behind that of the oscillating field $h(t)$ ($= h_0 \sin \omega t$, say), and after some initial transient period, the dynamic $m(t) - h(t)$ loop stabilizes and encloses a nonvanishing loop area $A(T, h_0, \omega) [= \oint m dh]$, which depends on the temperature T of the system and the field amplitude h_0 and frequency ω . This hysteresis is dynamical in origin and disappears in the quasistatic limit. Pure magnetic systems, without any random defects or anisotropies to pin the magnetic domains, can relax properly in the quasistatic limit and follow the field in phase due to the presence of thermal fluctuations at any finite temperature. No hysteresis can therefore occur in pure magnets in the quasistatic limit [27, 57-58].

A power-law dependence of such hysteretic loss on the magnetic induction (related to the external field) was first proposed empirically, more than a century ago, by Steinmetz [59].

Typically, for fixed temperature T and field amplitude h_0 , the dynamic hysteresis loss A increases with increasing frequency ω for low values of ω . This is because, for low values of ω , the effective delay in the response increases as ω increases. In general, for a fixed ω , A increases with decreasing T and increasing h_0 until A saturates. Eventually, as the driving frequency exceeds a threshold value (dependent on h_0 and T [60]), the loop area A starts decreasing, because of the increase in the effective delay (phase lag) towards 2π , as seen Figure 2.17. Eventually, the loop area vanishes for very high frequencies when the dynamic symmetry is fully broken.

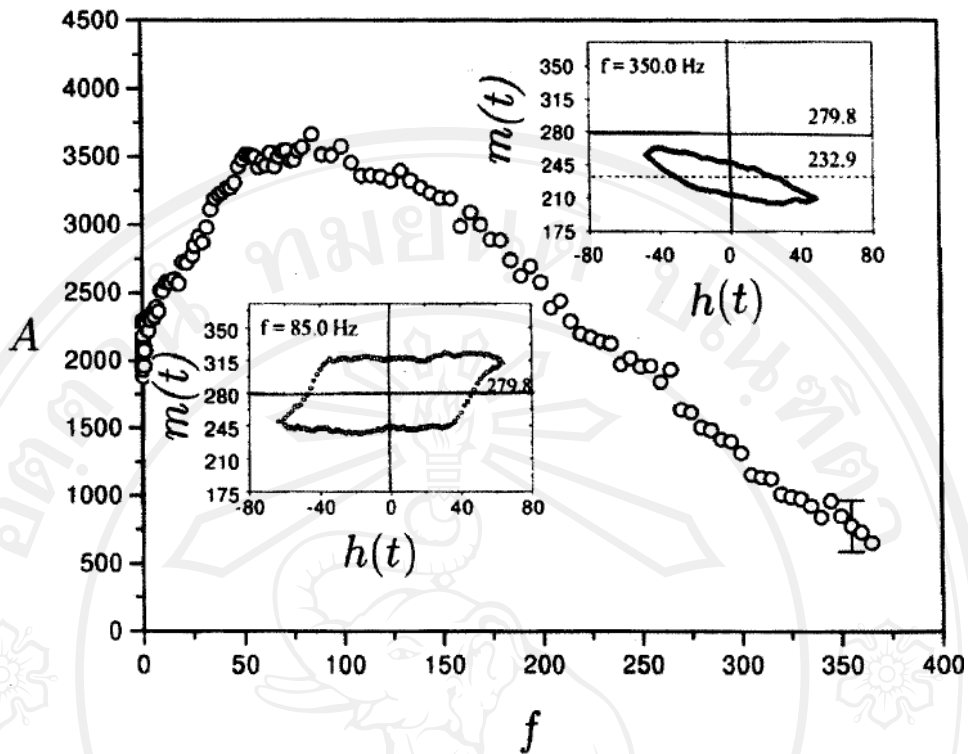


Figure 2.17 The frequency-dependent hysteresis area A of epitaxially grown ultrathin Co films on a Cu(001) surface at room temperature, the results for the loop area A as a function of frequency f is plotted at a fixed ac current of 0.4 Amp. The direction of the magnetic field is parallel to the film plane. The insets show plots of m - h loops for the following particular values of the field amplitudes h_0 : (i) $h_0 = 48.0$ Oe (top inset) and (ii) $h_0 = 63.0$ Oe (bottom inset) [55]

The dynamic contribution to the coercive field and the hysteresis loop area has been investigated in several recent experiments, mostly in thin films or in two dimensions. Bruno *et al.* [61] studied the dependence of the hysteresis loop area A on the rate of change of the external field, in ultrathin ferromagnetic films. Their study gives some indirect information on the dynamic contribution to the loop area A .

In a more recent experiment, Jiang *et al.* [9, 62-63] studied the frequency-dependent hysteresis of epitaxially grown ultrathin (2 to 6 monolayer thick) Co films

on a Cu (001) surface at room temperature. The films have strong uniaxial magnetization with two ferromagnetic phases of opposite spin orientations. This magnetic anisotropy makes it appropriate to represent the system by an Ising-like model (see also He and Wang [64]). The external magnetic field $h(t)$ on the system was driven sinusoidally in the frequency ($f = \omega/2\pi$) range 0.1 to 500 Hz and in the amplitude (h_0) range 1 to 180 Oe. Here of course the time-varying current or the magnetic field induces an eddy current in the core, which results in a counter-field reducing the effective magnitude of the applied field. The surface magneto-optical Kerr effect technique was used to measure the response magnetization $m(t)$. A typical variation of the loop area A with the driving frequency f , at room temperature and at fixed external field amplitude h_0 , is shown in Figure 2.17. Also, it may be mentioned that in a recent similar experiment on dynamic hysteresis in ultrathin Fe films on W(110) surface (Suen and Erskine [65]), the typical behavior of the dynamic hysteresis is observed to be similar, although considerable discrepancies are observed in the actual details for different materials and regimes.

The observed variation of the loop area A with frequency ω follows the generic form discussed earlier: A decreases for both low and high values of ω .

However, it may be noted that A does not quite vanish in the zero frequency limit. The observed variation can, in fact, be fitted to a form

$$A = A_0 + h_0^\alpha \omega^\beta g\left(\frac{\omega}{h_0^\gamma}\right), \quad (2.16)$$

with the scaling exponents α , β , and γ and with the scaling function g having a suitable nonmonotonic form such that $g(x) \rightarrow 0$ as $x \rightarrow 0$ or ∞ . Here A_0 is the loop area in the zero frequency limit. It seems, depending on the nature of the dynamic

processes involved in different materials and also the ranges (of amplitude, frequency, etc.), the values of the exponents differ dramatically. While Jiang *et al.* [9] obtained $\alpha \approx 0.67 \approx \beta$ for Co films on Cu (100), and $\alpha \approx 0.60$ and $\beta \approx 0.30$ for Fe films on Au (001), Suen and Erskine [65] obtained much lower values for the same exponents: $\alpha \approx 0.30$ and $\beta \approx 0.06$ (perhaps logarithmic) for Fe films on W (110) surfaces.

Similarly, the ferroelectric responses of ferroelectric materials under various perturbations are very same as magnetic responses of magnets, and moreover frequency and electric field are also basic parameters responsible for ferroelectric hysteresis of ferroelectric materials.

Therefore, the concept of power-law scaling relation used originally for magnetic materials is applied for ferroelectric materials case. Through some simplifications and parameter modifications, the power-law scaling relation for ferroelectric materials can be obtained in form of

$$\langle A \rangle \propto f^m E_0^n \quad (2.17)$$

(where m and n are exponents dependent on the dimensionality and symmetry of the system).

2.7 Data analysis

2.7.1 Least squares

The Method of Least Squares is a procedure to determine the best fit line to data; the proof uses calculus and linear algebra. The basic problem is to find the best fit straight line $y = ax + b$ given that, for $n \in \{1, \dots, N\}$, the pairs (x_n, y_n) are observed. The method easily generalizes to finding the best fit of the form

$$y = a_1 f_1(x) + \dots + c_K f_K(x) \quad (2.18)$$

it is not necessary for the functions f_K to be linearly in x — all that is needed is that y is to be a linear combination of these functions [66].

2.7.1.1 Probability and statistics review

We give a quick introduction to the basic elements of probability and statistics which we need for the Method of Least Squares; for more details see [67-73].

Given a sequence of data x_1, \dots, x_N , we define the mean (or the expected value) to be $(x_1 + \dots + x_N)/N$. We denote this by writing a line above x : thus

$$\bar{x} = \frac{1}{N} \sum_{n=1}^N x_n \quad (2.19)$$

The mean is the average value of the data.

Consider the following two sequences of data: $\{10, 20, 30, 40, 50\}$ and $\{30, 30, 30, 30\}$. Both sets have the same mean; however, the first data set has greater variation about the mean. This leads to the concept of variance, which is a useful tool to quantify how much a set of data fluctuates about its mean. The variance of $\{x_1, \dots, x_N\}$, denoted by σ_x^2 is

$$\sigma_x^2 = \frac{1}{N} \sum_{n=1}^N (x_i - \bar{x})^2 \quad (2.20)$$

the standard deviation σ_x is the square root of the variance:

$$\sigma_x = \sqrt{\frac{1}{N} \sum_{n=1}^N (x_i - \bar{x})^2} \quad (2.21)$$

Note that if the x 's have units of meters then the variance σ_x^2 has units of meters², and the standard deviation σ_x and the mean \bar{x} have units of meters. Thus it is the standard deviation that gives a good measure of the deviations of the x 's around their mean, as it has the same units as our quantity of interest.

There are, of course, alternate measures one can use. For example, one could consider

$$\frac{1}{N} \sum_{n=1}^N (x_n - \bar{x}) \quad (2.22)$$

Unfortunately this is a signed quantity, and large positive deviations can cancel with large negatives. In fact, the definition of the mean immediately implies the above is zero! This, then, would be a terrible measure of the variability in data, as it is zero regardless of what the values of the data are.

We can rectify this problem by using absolute values. This leads us to consider

$$\frac{1}{N} \sum_{n=1}^N |x_n - \bar{x}| \quad (2.23)$$

While this has the advantage of avoiding cancellation of errors (as well as having the same units as the x 's), the absolute value function is not a good function analytically. It is not differentiable. This is primarily why we consider the standard deviation (the square root of the variance) – this will allow us to use the tools from calculus.

We can now quantify what we mean by “best fit”. If we believe $y = ax + b$, then $y - (ax + b)$ should be zero. Thus given observations

$$\{(x_1, y_1), \dots, (x_N, y_N)\} \quad (2.24)$$

we look at

$$\{y_1 - (ax_1 + b), \dots, y_N - (ax_N + b)\} \quad (2.25)$$

The mean should be small (if it is a good fit), and the sum of squares of the terms will measure how good of a fit we have.

We define

$$E(a, b) := \sum_{n=1}^N (y_n - (ax_n + b))^2 \quad (2.26)$$

Large errors are given a higher weight than smaller errors (due to the squaring). Thus our procedure favors many medium sized errors over a few large errors. If we used absolute values to measure the error (see Equation (2.23)), then all errors are weighted equally; however, the absolute value function is not differentiable, and thus the tools of calculus become inaccessible.

2.7.1.2 The method of least squares

Given data $\{(x_1, y_1), \dots, (x_N, y_N)\}$, we defined the error associated to saying $y = ax + b$ by

$$E(a, b) := \sum_{n=1}^N (y_n - (ax_n + b))^2 \quad (2.27)$$

Note that the error is a function of two variables, the unknown parameters a and b .

The goal is to find values of a and b that minimize the error. In multivariable calculus we learn that this requires us to find the values of (a, b) such that the gradient of E with respect to our variables (which are a and b) vanishes; thus we require

$$\nabla E = \left(\frac{\partial E}{\partial a}, \frac{\partial E}{\partial b} \right) = (0, 0) \quad (2.28)$$

or

$$\frac{\partial E}{\partial a} = 0, \frac{\partial E}{\partial b} = 0 \quad (2.29)$$

Note we do not have to worry about boundary points: as $|a|$ and $|b|$ become large, the fit will clearly get worse and worse. Thus we do not need to check on the boundary.

Differentiating $E(a, b)$ yields

$$\begin{aligned} \frac{\partial E}{\partial a} &= \sum_{n=1}^N 2(y_n - (ax_n + b)) \cdot (-x_n) \\ \frac{\partial E}{\partial b} &= \sum_{n=1}^N 2(y_n - (ax_n + b)) \cdot (-1) \end{aligned} \quad (2.30)$$

Setting $\frac{\partial E}{\partial a} = \frac{\partial E}{\partial b} = 0$ (and dividing by -2) yields

$$\begin{aligned} \sum_{n=1}^N (y_n - (ax_n + b)) \cdot x_n &= 0 \\ \sum_{n=1}^N (y_n - (ax_n + b)) &= 0 \end{aligned} \quad (2.31)$$

Note we can divide both sides by -2 as it is just a constant; we cannot divide by x_i as that varies with i .

We may rewrite these equations as

$$\begin{aligned} (\sum_{n=1}^N x_n^2)a + (\sum_{n=1}^N x_n)b &= \sum_{n=1}^N x_n y_n \\ (\sum_{n=1}^N x_n)a + (\sum_{n=1}^N 1)b &= \sum_{n=1}^N y_n \end{aligned} \quad (2.32)$$

We have obtained that the values of a and b which minimize the error (defined in (2.27)) satisfy the following matrix equation:

$$\begin{pmatrix} \sum_{n=1}^N x_n^2 & \sum_{n=1}^N x_n \\ \sum_{n=1}^N x_n & N \end{pmatrix} \begin{pmatrix} a \\ b \end{pmatrix} = \begin{pmatrix} \sum_{n=1}^N x_n y_n \\ \sum_{n=1}^N y_n \end{pmatrix} \quad (2.33)$$

We need a fact from linear algebra. Recall the inverse of a matrix A is a matrix B such that $AB = BA = I$, where I is the identity matrix. If $A = \begin{pmatrix} \alpha & \beta \\ \gamma & \delta \end{pmatrix}$ is a 2×2 matrix where $\det A = \alpha\delta - \beta\gamma \neq 0$, then A is invertible and

$$A^{-1} = \frac{1}{\alpha\delta - \beta\gamma} \begin{pmatrix} \delta & -\beta \\ -\gamma & \alpha \end{pmatrix} \quad (2.34)$$

In other words, $AA^{-1} = \begin{pmatrix} 1 & 0 \\ 0 & 1 \end{pmatrix}$ here. For example, if $A = \begin{pmatrix} 1 & 2 \\ 3 & 7 \end{pmatrix}$ then $\det A = 1$ and $A^{-1} = \begin{pmatrix} 7 & -2 \\ -3 & 1 \end{pmatrix}$; we can check this by noting (through matrix multiplication) that

$$\begin{pmatrix} 1 & 2 \\ 3 & 7 \end{pmatrix} \begin{pmatrix} 7 & -2 \\ -3 & 1 \end{pmatrix} = \begin{pmatrix} 1 & 0 \\ 0 & 1 \end{pmatrix} \quad (2.35)$$

We can show the matrix in (2.33) is invertible (so long as at least two of the x_n 's are distinct), which implies

$$\begin{pmatrix} a \\ b \end{pmatrix} = \begin{pmatrix} \sum_{n=1}^N x_n^2 & \sum_{n=1}^N x_n \\ \sum_{n=1}^N x_n & N \end{pmatrix}^{-1} \begin{pmatrix} \sum_{n=1}^N x_n y_n \\ \sum_{n=1}^N y_n \end{pmatrix} \quad (2.36)$$

Denote the matrix from (2.33) by M . The determinant of M is

$$\det M = \sum_{n=1}^N x_n^2 \cdot \sum_{n=1}^N 1 - \sum_{n=1}^N x_n \cdot \sum_{n=1}^N x_n \quad (2.37)$$

As

$$\bar{x} = \frac{1}{N} \sum_{n=1}^N x_n \quad (2.38)$$

we find that

$$\det M = N \sum_{n=1}^N x_n^2 - (N\bar{x})^2$$

$$\begin{aligned}
&= N^2 \left(\frac{1}{N} \sum_{n=1}^N x_n^2 - \bar{x}^2 \right) \\
&= N^2 \cdot \frac{1}{N} \sum_{n=1}^N (x_n - \bar{x})^2
\end{aligned} \tag{2.39}$$

where the last equality follows from simple algebra. Thus, as long as all the x_n are not equal, $\det M$ will be non-zero and M will be invertible. Using the definition of variance, we notice the above could also be written as

$$\det M = N^2 \sigma_x^2 \tag{2.40}$$

Thus we find that, so long as the x 's are not all equal, the best fit values of a and b are obtained by solving a linear system of equations; the solution is given in Equation (2.36). We rewrite Equation (2.36) in a simpler form. Using the inverse of the matrix and the definition of the mean and variance, we find

$$\begin{pmatrix} a \\ b \end{pmatrix} = \frac{1}{N^2 \sigma_x^2} \begin{pmatrix} N & -N\bar{x} \\ -N\bar{x} & \sum_{n=1}^N x_n^2 \end{pmatrix} \begin{pmatrix} \sum_{n=1}^N x_n y_n \\ \sum_{n=1}^N y_n \end{pmatrix} \tag{2.41}$$

Expanding gives

$$a = \frac{N \sum_{n=1}^N x_n y_n - N\bar{x} \sum_{n=1}^N y_n}{N^2 \sigma_x^2}$$

$$b = \frac{-N\bar{x} \sum_{n=1}^N x_n y_n + \sum_{n=1}^N x_n^2 \sum_{n=1}^N y_n}{N^2 \sigma_x^2}$$

$$\bar{x} = \frac{1}{N} \sum_{n=1}^N x_i$$

$$\sigma_x^2 = \frac{1}{N} \sum_{n=1}^N (x_i - \bar{x})^2 \tag{2.42}$$

As the formulas for a and b are so important, it is worth giving another expression for them. We also have [66]

$$a = \frac{\sum_{n=1}^N 1 \sum_{n=1}^N x_n y_n - \sum_{n=1}^N x_n \sum_{n=1}^N y_n}{\sum_{n=1}^N 1 \sum_{n=1}^N x_n^2 - \sum_{n=1}^N x_n \sum_{n=1}^N x_n}$$

$$b = \frac{\sum_{n=1}^N x_n \sum_{n=1}^N x_n y_n - \sum_{n=1}^N x_n^2 \sum_{n=1}^N y_n}{\sum_{n=1}^N x_n \sum_{n=1}^N x_n - \sum_{n=1}^N x_n^2 \sum_{n=1}^N 1} \quad (2.43)$$

2.7.2 Coefficient of determination

In statistics, the coefficient of determination R^2 is used in the context of statistical models whose main purpose is the prediction of future outcomes on the basis of other related information. It is the proportion of variability in a data set that is accounted for by the statistical model [74]. It provides a measure of how well future outcomes are likely to be predicted by the model.

There are several different definitions of R^2 which are only sometimes equivalent. One class of such cases includes that of linear regression. In this case, if an intercept is included then R^2 is simply the square of the sample correlation coefficient between the outcomes and their predicted values, or in the case of simple linear regression, between the outcomes and the values of the single regressor being used for prediction. In such cases, the coefficient of determination ranges from 0 to 1. Important cases where the computational definition of R^2 can yield negative values, depending on the definition used, arise where the predictions which are being compared to the corresponding outcomes have not been derived from a model-fitting procedure using those data, and where linear regression is conducted without including an intercept. Additionally, negative values of R^2 may occur when fitting non-linear trends to data [75]. In these instances, the mean of the data provides a fit to the data that is superior to that of the trend under this goodness of fit analysis.

Definitions

A data set has values y_i , each of which has an associated modelled value f_i (also sometimes referred to as \hat{y}_i). Here, the values y_i are called the observed values and the modelled values f_i are sometimes called the predicted values.

The "variability" of the data set is measured through different sums of squares:

$SS_{tot} = \sum_i (y_i - \bar{y})^2$, the total sum of squares (proportional to the sample variance),

$SS_{reg} = \sum_i (f_i - \bar{y})^2$, the regression sum of squares, also called the explained sum of squares,

$SS_{err} = \sum_i (y_i - f_i)^2$, the sum of squares of residuals, also called the residual sum of squares.

In the above \bar{y} is the mean of the observed data:

$$\bar{y} = \frac{1}{n} \sum_i^n y_i \quad (2.44)$$

where n is the number of observations.

The most general definition of the coefficient of determination is

$$R^2 \equiv 1 - \frac{SS_{err}}{SS_{tot}} \quad (2.45)$$

Relation to unexplained variance

In a general form, R^2 can be seen to be related to the unexplained variance, since the second term compares the unexplained variance (variance of the model's errors) with the total variance (of the data).

As explained variance

In some cases the total sum of squares equals the sum of the two other sums of squares defined above,

$$SS_{err} + SS_{reg} = SS_{tot} \quad (2.46)$$

When this relation does hold, the above definition of R^2 is equivalent to

$$R^2 = \frac{SS_{reg}}{SS_{tot}} \quad (2.47)$$

In this form R^2 is given directly in terms of the explained variance: it compares the explained variance (variance of the model's predictions) with the total variance (of the data). This partition of the sum of squares holds for instance when the model values f_i have been obtained by linear regression. A milder sufficient condition reads as follows: The model has the form

$$f_i = \alpha + \beta q_i \quad (2.48)$$

where the q_i are arbitrary values that may or may not depend on i or on other free parameters (the common choice $q_i = x_i$ is just one special case), and the coefficients α and β are obtained by minimizing the residual sum of squares.

This set of conditions is an important one and it has a number of implications for the properties of the fitted residuals and the modelled values. In particular, under these conditions:

$$\bar{f} = \bar{y} \quad (2.49)$$

As squared correlation coefficient

Similarly, after least squares regression with a constant linear model, R^2 equals the square of the correlation coefficient between the observed and modeled (predicted) data values.

Under general conditions, an R^2 value is sometimes calculated as the square of the correlation coefficient between the original and modeled data values. In this case, the value is not directly a measure of how good the modeled values are, but rather a measure of how good a predictor might be constructed from the modeled values (by creating a revised predictor of the form $\alpha + \beta f_i$). According to Everitt [76], this usage is specifically the definition of the term "coefficient of determination": the square of the correlation between two (general) variables.

Interpretation

R^2 is a statistic that will give some information about the goodness of fit of a model. In regression, the R^2 coefficient of determination is a statistical measure of how well the regression line approximates the real data points. An R^2 of 1.0 indicates that the regression line perfectly fits the data.

Values of R^2 outside the range 0 to 1 can occur where it is used to measure the agreement between observed and modelled values and where the "modelled" values are not obtained by linear regression and depending on which formulation of R^2 is used. If the first formula above is used, values can never be greater than one. If the second expression is used, there are no constraints on the values obtainable.

In many (but not all) instances where R^2 is used, the predictors are calculated by ordinary least-squares regression: that is, by minimizing SS_{err} . In this case R -squared increases as we increase the number of variables in the model (R^2 will not

decrease). This illustrates a drawback to one possible use of R^2 , where one might try to include more variables in the model until "there is no more improvement". This leads to the alternative approach of looking at the adjusted R^2 . The explanation of this statistic is almost the same as R^2 but it penalizes the statistic as extra variables are included in the model. For cases other than fitting by ordinary least squares, the R^2 statistic can be calculated as above and may still be a useful measure. If fitting is by weighted least squares or generalized least squares, alternative versions of R^2 can be calculated appropriate to those statistical frameworks, while the "raw" R^2 may still be useful if it is more easily interpreted. Values for R^2 can be calculated for any type of predictive model, which need not have a statistical basis.

Adjusted R^2

Adjusted R^2 (often written as \bar{R}^2 and pronounced "R bar squared") is a modification of R^2 that adjusts for the number of explanatory terms in a model. Unlike R^2 , the adjusted R^2 increases only if the new term improves the model more than would be expected by chance. The adjusted R^2 can be negative, and will always be less than or equal to R^2 . The adjusted R^2 is defined as

$$\bar{R}^2 = 1 - (1 - R^2) \frac{n-1}{n-p-1} = 1 - R^2 \equiv 1 - \frac{SS_{err} df_t}{SS_{tot} df_e} \quad (2.50)$$

where p is the total number of regressors in the linear model (but not counting the constant term), n is the sample size, df_t is the degrees of freedom $n - 1$ of the estimate of the population variance of the dependent variable, and df_e is the degrees of freedom $n - p - 1$ of the estimate of the underlying population error variance.

The principle behind the Adjusted R^2 statistic can be seen by rewriting the ordinary R^2 as

$$R^2 = 1 - \frac{VAR_{err}}{VAR_{tot}} \quad (2.51)$$

where $VAR_{err} = SS_{err} / n$ and $VAR_{tot} = SS_{tot} / n$ are estimates of the variances of the errors and of the observations, respectively. These estimates are replaced by statistically unbiased versions: $VAR_{err} = SS_{err} / (n - p - 1)$ and $VAR_{tot} = SS_{tot} / (n - 1)$.

Adjusted R^2 does not have the same interpretation as R^2 . As such, care must be taken in interpreting and reporting this statistic. Adjusted R^2 is particularly useful in the feature selection stage of model building. The use of an adjusted R^2 is an attempt to take account of the phenomenon of statistical shrinkage [76].

Generalized R^2

Nagelkerke [77] generalizes the definition of the coefficient of determination:

1. A generalized coefficient of determination should be consistent with the classical coefficient of determination when both can be computed.
2. Its value should also be maximized by the maximum likelihood estimation of a model.
3. It should be, at least asymptotically, independent of the sample size.
4. Its interpretation should be the proportion of the variation explained by the model.
5. It should be between 0 and 1, with 0 denoting that model does not explain any variation and 1 denoting that it perfectly explains the observed variation.
6. It should not have any unit.

The generalized R^2 has all of these properties.

$$R^2 = 1 - \left(\frac{L(0)}{L(\hat{\theta})}\right)^{2/n} \quad (2.52)$$

where $L(0)$ is the likelihood of the model with only the intercept, $L(\hat{\theta})$ is the likelihood of the estimated model and n is the sample size.

However, in the case of a logistic model, where $L(\hat{\theta})$ cannot be greater than 1, R^2 is between 0 and $R_{max}^2 = 1 - (L(0))^{2/n}$: thus, it is possible to define a scaled R^2 as R^2/R_{max}^2 [78].

2.7.3 Fourier transform

The sufficiently smooth function $f(t)$ that is periodic can be built out of sin's and cos's. We have seen that complex exponentials may be used in place of sin's and cos's. We shall now use complex exponentials because they lead to less writing and simpler computations, but yet can easily be converted into sin's and cos's. If $f(t)$ has period $2l$, its (complex) Fourier series expansion is [79]

$$f(t) = \sum_{k=-\infty}^{\infty} c_k e^{ik\frac{\pi}{l}t} \text{ with } c_k = \frac{1}{2l} \int_{-l}^l f(t) e^{-ik\frac{\pi}{l}t} dt \quad (2.53)$$

Not surprisingly, each term $c_k e^{ik\frac{\pi}{l}t}$ in this expansion also has period $2l$, because $c_k e^{ik\frac{\pi}{l}(t+2l)} = c_k e^{ik\frac{\pi}{l}t} e^{i2k\pi} = c_k e^{ik\frac{\pi}{l}t}$. We now develop an expansion for non-periodic functions, by allowing complex exponentials (or equivalently sin's and cos's) of all possible periods, not just $2l$, for some fixed l . So, from now on, do not assume that $f(t)$ is periodic.

For simplicity we will only develop the expansions for functions that are zero for all sufficiently large $|t|$. With a little more work, one can show that our conclusions

apply to a much broader class of functions. Let $L > 0$ be sufficiently large that $f(t) = 0$ for all $|t| \geq L$. We can get a Fourier series expansion for the part of $f(t)$ with $-L < t < L$ by using the periodic extension trick. Define $F_L(t)$ to be the unique function determined by the requirements that

- i) $F_L(t) = f(t)$ for $-L < t \leq L$
- ii) $F_L(t)$ is periodic of period $2L$

Then, for $-L < t < L$,

$$f(t) = F_L(t) = \sum_{k=-\infty}^{\infty} c_k(L) e^{ik\frac{\pi}{L}t} \quad \text{where} \quad c_k(L) = \frac{1}{2L} \int_{-L}^L f(t) e^{-ik\frac{\pi}{L}t} dt \quad (2.54)$$

If we can somehow take the limit $L \rightarrow \infty$, we will get a representation of f that is valid for all t 's, not just those in some finite interval $-L < t < L$. This is exactly what we shall do, by the simple expedient of interpreting the sum in Equation (2.54) as a Riemann sum approximation to a certain integral. For each integer k , define the k^{th} frequency to be $\omega_k = k\frac{\pi}{L}$ and denote by $\Delta\omega = \frac{\pi}{L}$ the spacing, $\omega_{k+1} - \omega_k$, between any two successive frequencies. Also define $\hat{f}(\omega) = \int_{-\infty}^{\infty} f(t) e^{-i\omega t} dt$. Since $f(t) = 0$ for all $|t| \geq L$

$$\begin{aligned} c_k(L) &= \frac{1}{2L} \int_{-L}^L f(t) e^{-ik\frac{\pi}{L}t} dt = \frac{1}{2L} \int_{-\infty}^{\infty} f(t) e^{-i\left(k\frac{\pi}{L}\right)t} dt = \frac{1}{2L} \int_{-\infty}^{\infty} f(t) e^{-i\omega_k t} dt \\ &= \frac{1}{2L} \hat{f}(\omega_k) = \frac{1}{2\pi} \hat{f}(\omega_k) \Delta\omega \end{aligned} \quad (2.55)$$

In this notation,

$$f(t) = F_L(t) = \frac{1}{2\pi} \sum_{k=-\infty}^{\infty} \hat{f}(\omega_k) e^{i\omega_k t} \Delta\omega \quad (2.56)$$

for any $-L < t < L$. As we let $L \rightarrow \infty$, the restriction $-L < |t| < L$ disappears, and the right hand side converges exactly to the integral $\frac{1}{2\pi} \int_{-\infty}^{\infty} \hat{f}(\omega) e^{i\omega t} d\omega$. To see this, cut the domain of integration into small slices of width $\Delta\omega$ and approximate, as in Figure 2.18, the area under the part of the graph of $\frac{1}{2\pi} \hat{f}(\omega) e^{i\omega t}$ with ω between ω_k and $\omega_k + \Delta\omega$ by the area of a rectangle of base $\Delta\omega$ and height $\frac{1}{2\pi} \hat{f}(\omega_k) e^{i\omega_k t}$.

This approximates the integral $\frac{1}{2\pi} \int_{-\infty}^{\infty} \hat{f}(\omega) e^{i\omega t} d\omega$ by the sum $\frac{1}{2\pi} \sum_{k=-\infty}^{\infty} \hat{f}(\omega_k) e^{i\omega_k t} \Delta\omega$. As $L \rightarrow \infty$ the approximation gets better and better so that the sum approaches the integral. So taking the limit of Equation (2.56) as $L \rightarrow \infty$ gives

$$f(t) = \frac{1}{2\pi} \int_{-\infty}^{\infty} \hat{f}(\omega) e^{i\omega t} d\omega \quad \text{where} \quad \hat{f}(\omega) = \int_{-\infty}^{\infty} f(t) e^{-i\omega t} dt \quad (2.57)$$

The function \hat{f} is called the Fourier transform of f . It is to be thought of as the frequency profile of the signal $f(t)$.

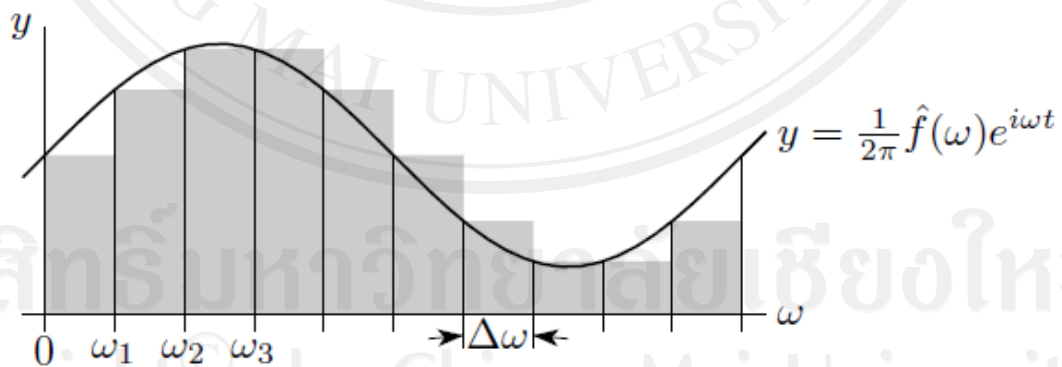


Figure 2.18 Integration forsliced domains of width $\Delta\omega$ [79]

2.8 Barium titanate (BT)

Barium titanate, the first ceramic material in which ferroelectric behavior was observed, is the ideal model for a discussion of the phenomenon from the point of view of crystal structure and microstructure [80].

BaTiO₃ is isostructural with the mineral perovskite (CaTiO₃) and so is referred to as 'a perovskite'. The generalized perovskite structure ABO₃, is visualized as based on a cubic close-packed assembly of composition AO₃ with the A-ion coordinated with 12 oxygen ions and the B-ion in the octahedral interstices (see Figure 2.19). A consideration of the geometry shows that for a perfect fit the following relationship between the ionic radii holds [81].

$$R_A + R_O = 2(R_B + R_O) \quad (2.58)$$

For the many compounds having the perovskite structure the relationship will not hold exactly because of small variations in the sizes of the A and B ions. Therefore, to allow for this Equation (2.58) is written

$$R_A + R_O = t2(R_B + R_O) \quad (2.59)$$

in which '*t*' is termed the 'tolerance factor' with a value typically in the range $0.95 < t < 1.06$. In the case of SrTiO₃ $t = 1$. When $t \neq 1$ then small lattice distortions (the octahedra tilt) occur in order to minimize lattice energy. These distortions have a significant effect on dielectric properties.

Above its Curie point (approximately 130 °C) the unit cell is cubic with the ions arranged as in Figure 2.19. Below the Curie point the structure is slightly distorted to the tetragonal form with a dipole moment along the *c* direction. Other

transformations occur at temperatures close to 0 °C and -80 °C: below 0 °C the unit cell is orthorhombic with the polar axis parallel to a face diagonal and below -80 °C it is rhombohedral with the polar axis along a body diagonal.

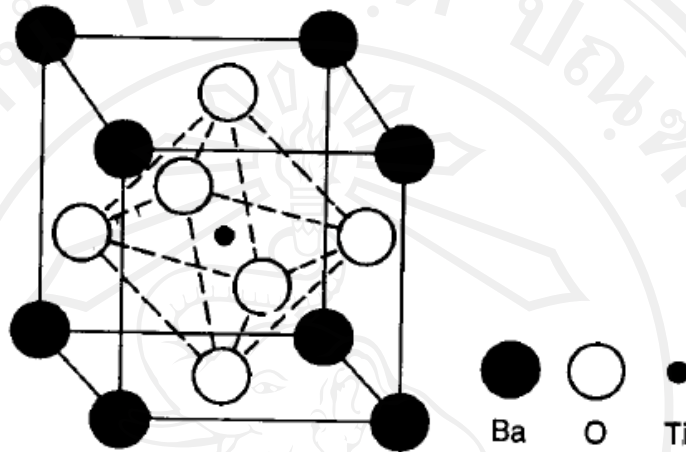
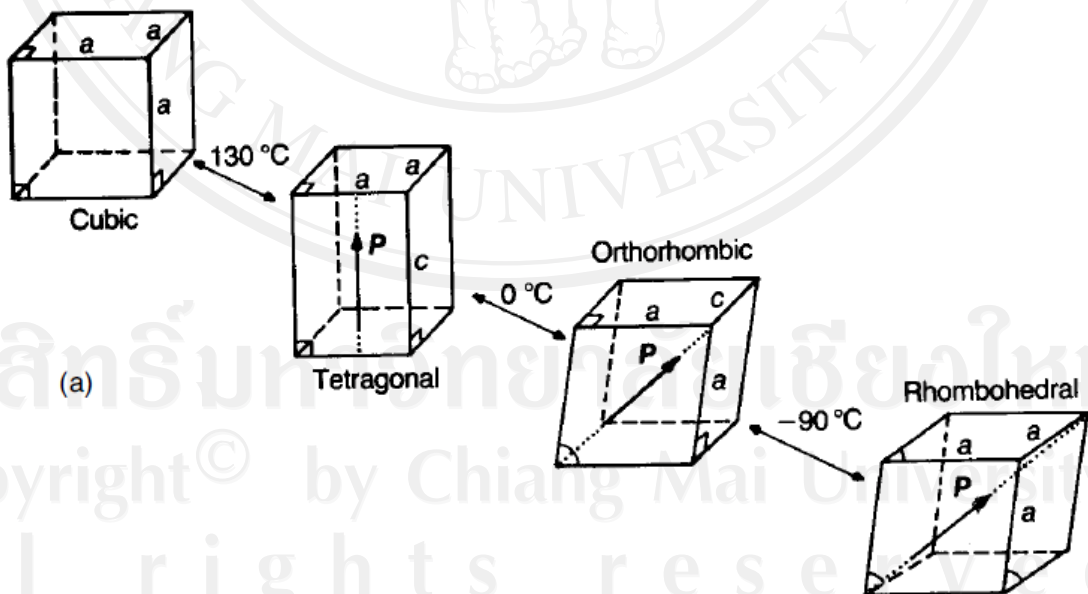
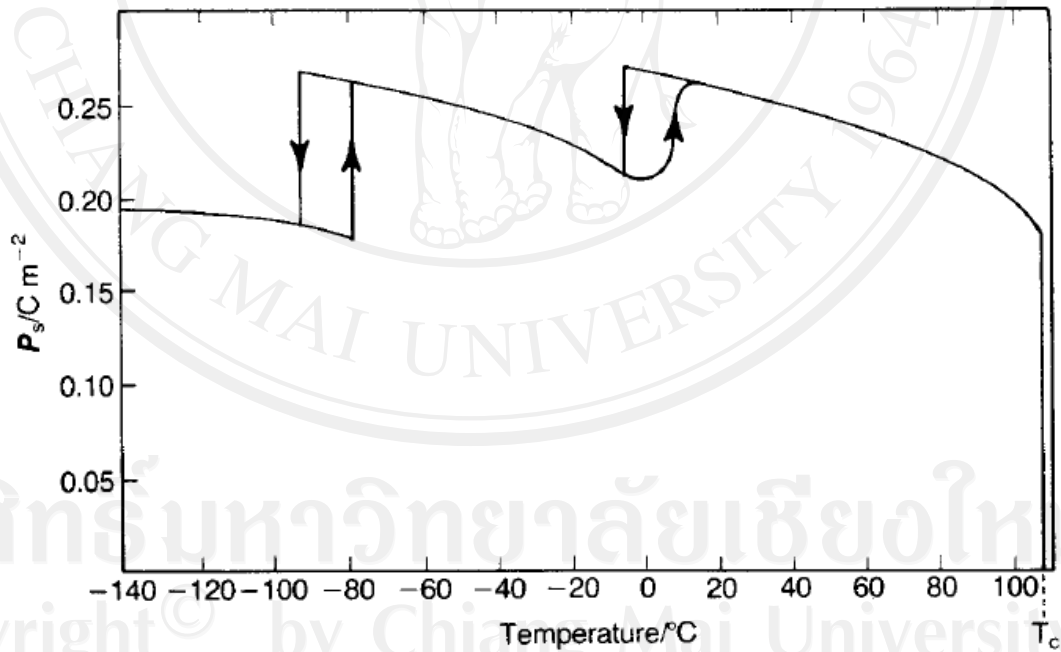
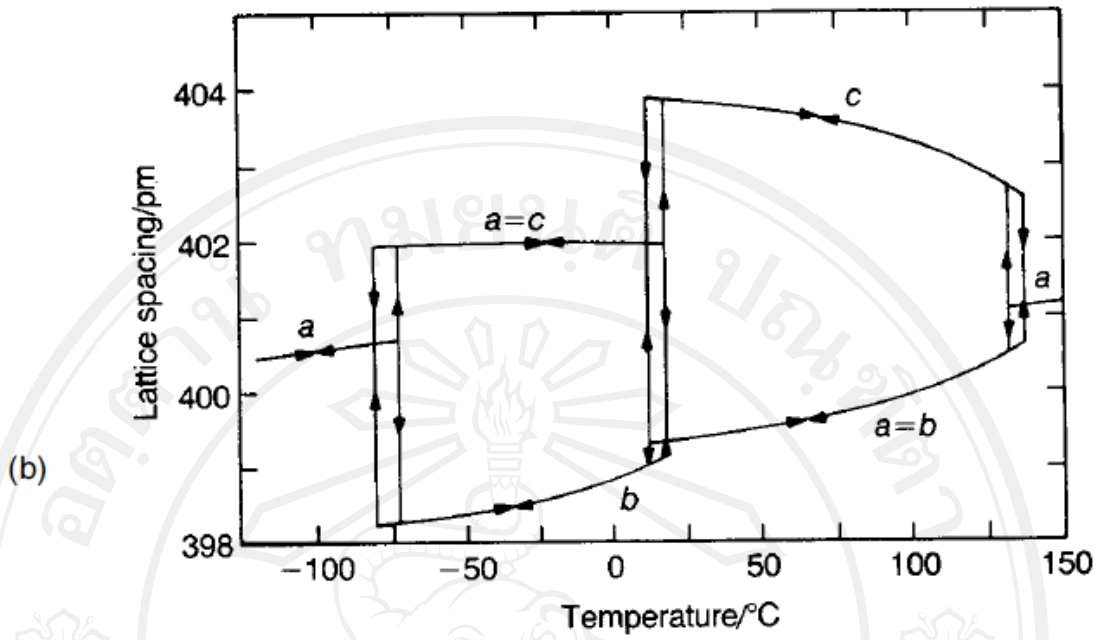
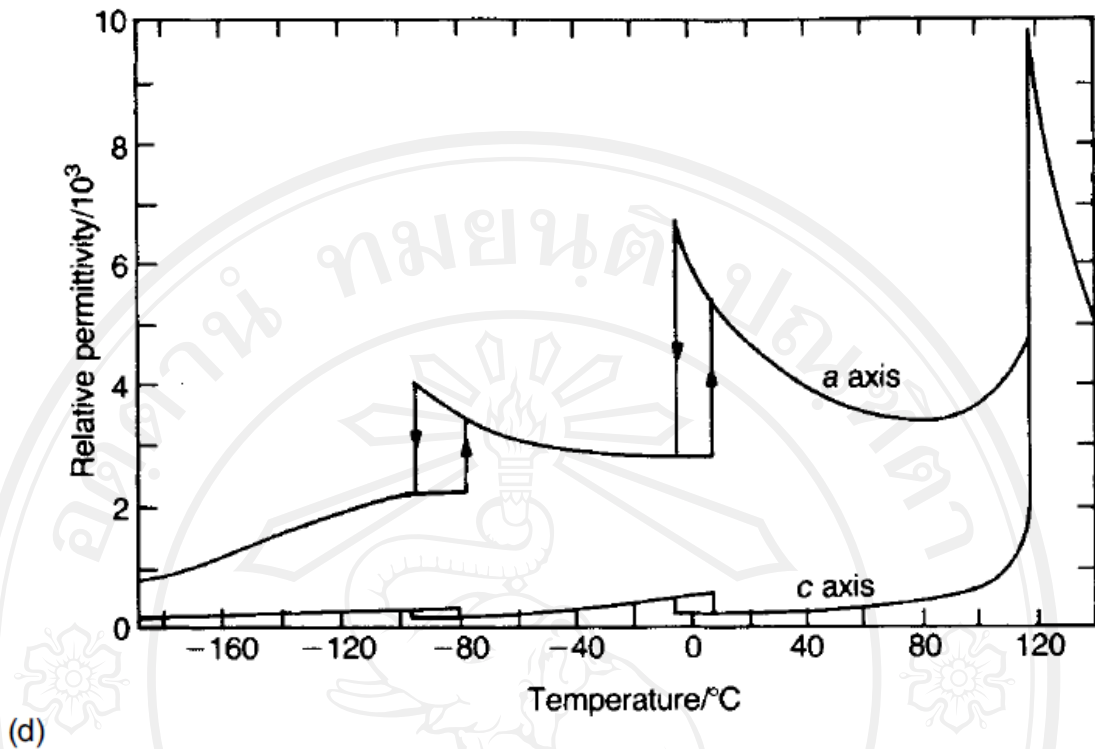


Figure 2.19 The unit cell of BaTiO₃ [80]







(d) **Figure 2.20** Properties of single-crystal BaTiO₃: (a) unit-cell distortions of the polymorphs; (b) lattice dimensions versus temperature (after R. Clarke J. Appl. Cryst. 9, 335, 1976); (c) spontaneous polarization versus temperature; (d) relative permittivities measured in the *a* and *c* directions versus temperature (after W.J. Merz Phys. Rev. 76, 1221, 1949) [80]

The transformations are illustrated in Figure 2.20(a), and the corresponding changes in the values of the lattice parameters, the spontaneous polarization and the relative permittivity are shown in Figure 2.20(b–d).

A consideration of the ion displacements accompanying the cubic–tetragonal transformation can give insight into how the spontaneous polarization might be coupled from unit cell to unit cell. X-ray studies have established that in the tetragonal form, taking the four central (B) oxygen ions in the cubic phase as origin, the other ions are slightly shifted as shown in Figure 2.21. It is evident that if the central Ti⁴⁺

ion is closer to one of the O^{2-} ions marked A, it will be energetically favorable for the Ti^{4+} ion on the opposite side of A to be located more distantly from that O^{2-} ion, thus engendering a similar displacement of all the Ti^{4+} ions in a particular column in the same direction. Coupling between neighboring columns occurs in $BaTiO_3$ so that all the Ti^{4+} ions are displaced in the same direction. In contrast, in the orthorhombic perovskite $PbZrO_3$ the Zr^{4+} ions in neighboring columns are displaced in opposite senses so that the overall dipole moment is zero. Such a structure is termed antiferroelectric if the material shows a Curie point.

In tetragonal $BaTiO_3$ the energy of the Ti^{4+} ion in terms of its position along the c axis takes the form of two wells (Figure 2.22). An applied field in the opposite direction to the polarization may enable a Ti^{4+} ion to pass over the energy barrier between the two states and so reverse the direction of the polarity at that point. When this happens the energy barriers for neighboring ions are reduced and the entire region affected by the field will eventually switch into the new direction. A similar mechanism is available for changes of polarity through 90° but in this case there is an accompanying dimensional change because the polar c axis is longer than the non-polar a axis (Figure 2.20(b)). Switching through 90° can be induced through the ferroelastic effect by applying a compressive stress along the polar axis without an accompanying electric field. Mechanical stress does not induce 180° switching.

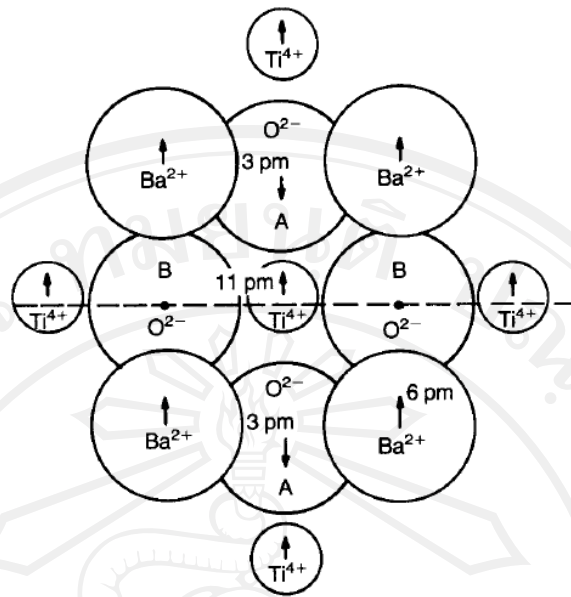


Figure 2.21 Approximate ion displacements in the cubic–tetragonal distortion in BaTiO_3 [80]

An immediate consequence of the onset of spontaneous polarization in a body is the appearance of an apparent surface charge density and an accompanying depolarizing field E_D as shown in Figure 2.23(a). The energy associated with the polarization in the depolarizing field is minimized by twinning, a process in which the crystal is divided into many oppositely polarized regions, as shown in Figure 2.23(b).

These regions are called domains and the whole configuration shown comprises 180° domains. Thus the surface consists of a mosaic of areas carrying apparent charges of opposite sign, resulting in a reduction in E_D and in energy. This multidomain state can usually be transformed into a single domain by applying a field parallel to one of the polar directions. The domains with their polar moment in the field direction grow at the expense of those directed oppositely until only a single domain remains. The presence of mechanical stress in a crystal results in the development of 90° domains

configured so as to minimize the strain. For example, as ceramic BaTiO_3 cools through the Curie temperature individual crystallites are subjected to large mechanical stresses leading to the development of 90° domains. The configurations can be modified by imposing either an electric or a mechanical stress. A polycrystalline ceramic that has not been subjected to a static field behaves as a non-polar material even though the crystals comprising it are polar. One of the most valuable features of ferroelectric behavior is that ferroelectric ceramics can be transformed into polar materials by applying a static field. This process is called 'poling'. The ceramic can be depoled by the application of appropriate electric fields or mechanical stresses. These poling and depoling processes are illustrated in Figure 2.24.

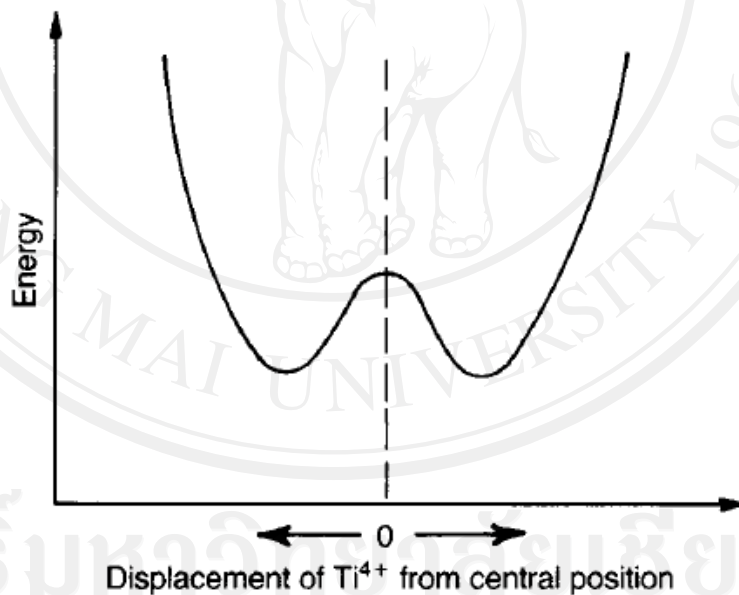


Figure 2.22 Variation in the potential energy of Ti^{4+} along the c axis [80]

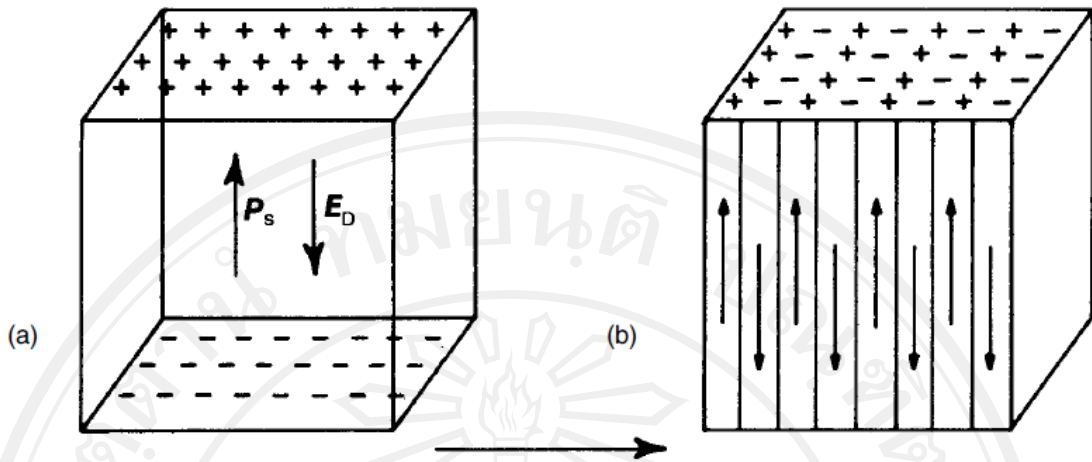


Figure 2.23 (a) Surface charge associated with spontaneous polarization; (b) formation of 180° domains to minimize electrostatic energy [80]

The random directions of the crystallographic axes of the crystallites of a ceramic limit the extent to which spontaneous polarization can be developed. It has been calculated that the fractions of the single-crystal polarization value that can be attained in a ceramic in which the polar axes take all possible alignments are 0.83, 0.91 and 0.87 for perovskites with tetragonal, orthorhombic or rhombohedral structures respectively. In ceramic tetragonal BaTiO_3 the saturation polarization is about half the single-crystal value. The value attainable is limited by the inhibition of 90° switching because of the strains involved, although 180° switching can be almost complete.

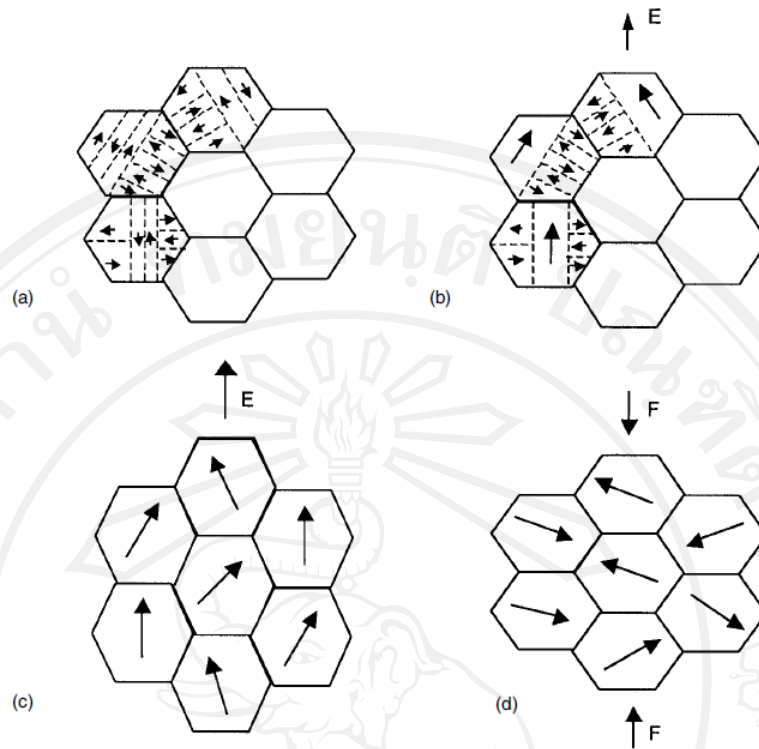


Figure 2.24 Schematic illustrating the changes accompanying the application of electrical and mechanical stresses to a polycrystalline ferroelectric ceramic: (a) stress-free – each grain is non-polar because of the cancellation of both 180° and 90° domains; (b) with applied electric field – 180° domains switch producing net overall polarity but no dimensional change; (c) with increase in electric field 90° domains switch accompanied by small ($\sim 1\%$) elongation; (d) domains disorientated by application of mechanical stress (Note the blank grains in (a) and (b) would contain similar domain structures) [80].

The domain structure revealed by polishing and etching an unpoled ceramic specimen is shown in Figure 2.25(a). The principal features in the form of parallel lines are due to 90° changes in the polar direction. The orientations occurring in a simple domain structure are shown schematically in Figure 2.25(b). The thickness of

the layer separating the domains, i.e. the domain wall, is of the order of 10 nm but varies with temperature and crystal purity. The wall energy is of the order 10 mJm^{-2} . The physics of domain formation and stress-relief is reviewed by G. Arlt [33].

The detailed geometry and dynamics of changes in domain configuration in a single crystal accompanying changes in applied field are complex and there is marked hysteresis between induced polarization and an applied field of sufficient strength. Conditions in a crystallite clamped within a ceramic are even more complex.



(a)

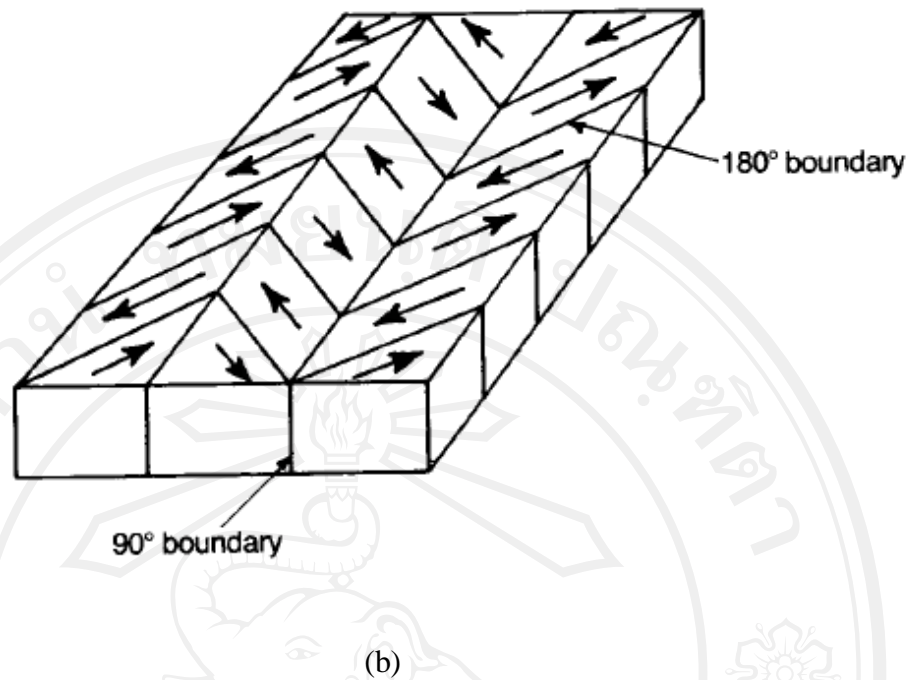


Figure 2.25 (a) Polished and etched surface of unpoled ceramic; (b) schematic diagram of 180° and 90° domains in barium titanate [80]

The hysteresis loop of a single-domain single crystal of BaTiO_3 is shown in Figure 2.26(a). The almost vertical portions of the loop are due to the reversal of the spontaneous polarization as reverse 180° domains nucleate and grow. The almost horizontal portions represent saturated states in which the crystal is single domain with a permittivity ϵ_r of 160 (see Figure 2.20(d)) measured in the polar direction. The coercive field at room temperature when the loop is developed by a 50 Hz supply is 0.1 MVm^{-1} and the saturation polarization is 0.27 Cm^{-2} . For fields in the approximate range 10 to 100 Vmm^{-1} the hysteresis loop takes the form of a narrow ellipse, a Rayleigh loop, with its major axis parallel to the almost horizontal part of the fully developed loop.

The hysteresis loop of a ceramic varies according to composition and ceramic structure but is typically of the form shown in Figure 2.26(b). The coercive field is higher and the remanent polarization is lower than for a single crystal. Changes in both 180° and 90° domain configurations take place during a cycle and are impeded by the defects and internal strains within the crystallites.

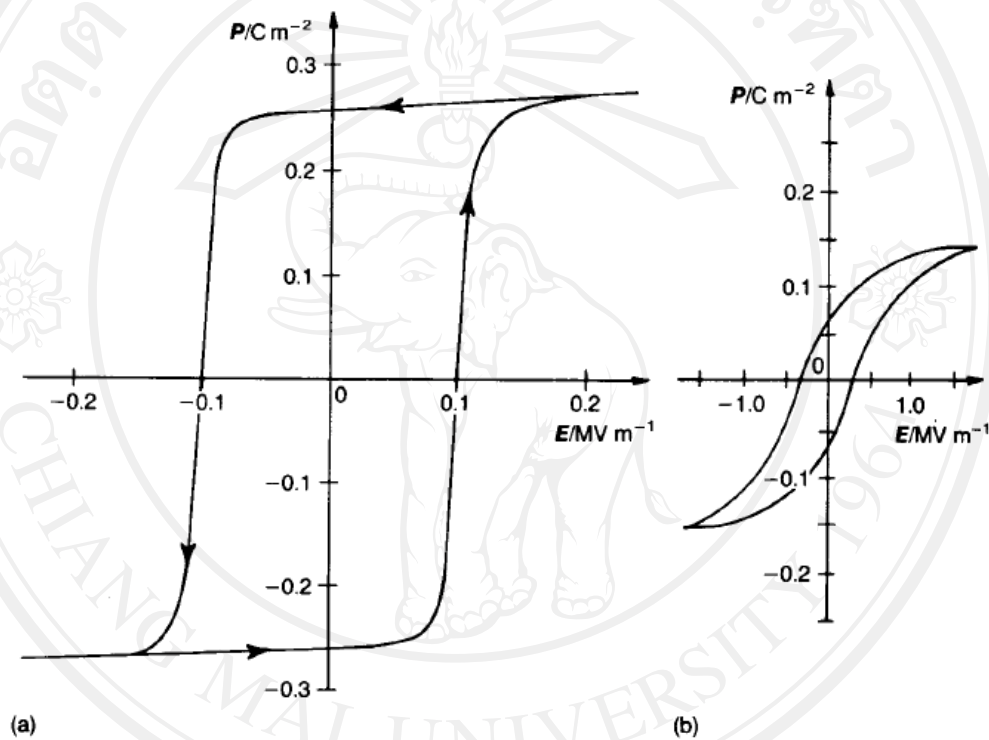


Figure 2.26 Hysteresis loops for (a) a single-domain single crystal of BaTiO_3 and (b) BaTiO_3 ceramic [80]

In discussing dielectric losses in ferroelectrics, it is necessary to distinguish between three mechanisms. The first involves the vibrating domain wall, the second a limited translation of the wall and the third the switching of the polarization direction of an entire domain. These three mechanisms are now discussed in a little more detail

when it is assumed that the driving electric field is sinusoidal and that when field strengths are referred to it is the amplitude which is the relevant parameter.

Considering first the vibrating domain wall, the losses have their origin in the emission of acoustic shear waves resulting from small changes in domain shape induced by the applied field. These losses are present at all frequencies extending up to the GHz range. At around 1 GHz there is a marked Debye-like relaxation effect with the losses reaching a maximum. The process bears a formal similarity to that discussed earlier. At this frequency the wavelength of an acoustic wave is of the same order of size as that of the domains (i.e. $\sim 1 \mu\text{m}$) and there will be strong scattering. The topic is discussed by G. Arlt and co-workers (e.g. [82]).

This loss mechanism is dominant up to a ‘threshold field’ (E_{th}) the strength of which depends upon the ‘softness’ or ‘hardness’ of the ferroelectric. Anticipating the later discussion of the family of piezoelectric ceramics ($\text{PbZrO}_3 - \text{PbTiO}_3$ [‘PZT’]) ‘hardness’ is engineered through specific doping which has the effect of ‘pinning’ the domain walls. The losses ($\tan \delta$) of a ‘hard’ and ‘soft’ PZT in the low field region (below E_{th}) are typically 0.003 and 0.02 respectively.

Above E_{th} the field is sufficiently strong to cause limited translation of the domain wall without disturbing to any significant extent the overall domain structure. This process is described as ‘reversible’ (more correctly as ‘nearly reversible’) to distinguish it from the very hysteretic and clearly irreversible process evidenced by the hysteresis loop (Figure 2.26). In this regime the P - E characteristic is a narrow loop, the Rayleigh loop referred to above.

When a critical field (E_C) is reached, which is near to the coercive field, the domains switch direction as a whole involving considerable hysteresis loss. This loss

is proportional to the area of the loop, so that for the single crystal in Figure 2.26(a) it amounts to about 0.1 MJm^{-3} . At 100 Hz the power dissipated as heat would be 100 MW-m^{-3} , which would result in a very rapid rise in temperature. The dissipation factor ($\tan \delta$) is also very high at high field strengths, but becomes small at low field strengths, as described above. Modifications to the composition diminish the loss still further. Dielectric hysteresis in the commercially important ferroelectric piezoceramics (e.g. 'PZT') is comprehensively reviewed by D. Hall [83].

2.9 Lead magnesium niobate-lead titanate (PMN-PT)

2.9.1 Lead magnesium niobate (PMN)

Lead magnesium niobate, $\text{Pb}(\text{Mg}_{1/3}\text{Nb}_{2/3})\text{O}_3$ or PMN, was first fabricated by Smolenskii and Agranovskaya [84] in the late 1950s and is one of the most studied of the complex lead-based perovskites. At room temperature, PMN exhibits a cubic perovskite structure with space group $Pm\bar{3}m$ and lattice constant $a = 4.04 \text{ \AA}$ [85]. On cooling, this high temperature paraelectric phase undergoes a gradual transition into a rhombohedral ferroelectric state over a wide range of temperatures centered at approximately $0 \text{ }^\circ\text{C}$. The origin of this broad dielectric response is postulated as caused by a distribution of Curie points resulting from microcompositional fluctuation in the B-site cations [86].

Pure lead magnesium niobate (PMN) [87-88] is a representative of relaxor ferroelectric materials with a transition temperature of $-10 \text{ }^\circ\text{C}$, at 1 kHz. There is cation disorder in the B-site for $\text{Pb}(\text{Mg}_{1/3}\text{Nb}_{2/3})\text{O}_3$ [89-91]. The composition regarding Mg/Nb ratio is not stoichiometric in the micro/nano-regions, leading to different ferroelectric transition temperatures which enhances the dielectric peak broadening. However, there have been many models proposed to explain the behavior of the

relaxor ferroelectric, for example, the inhomogeneous micro/nano-region model, the micro-micro domain transition model, the super paraelectric model, the dipolar glass model, the order-disorder model and etc. [91-94].

2.9.2 Lead titanate (PT)

Lead titanate (PbTiO_3 or PT) is a ferroelectric with a high Curie point ($\sim 490^\circ\text{C}$) at which the phase transition from the cubic paraelectric (above Curie point) to the tetragonal ferroelectric phase (below Curie point) occurs [85]. At room temperature, PT has a symmetry of point group $4mm$ with the ratio of axes $c/a \sim 1.063$, which is larger than that ($c/a \sim 1.01$) for barium titanate [80, 95]. It is very appropriate for high frequency and high temperature applications in electronics and microelectronics, due to its desirable dielectric constant ($\epsilon_r \sim 200$), pyroelectric, and piezoelectric ($k_r/k_p > 10$) properties [2, 80, 85]. It has been extensively employed to make solid solutions with lead zirconate (PbZrO_3) to obtain lead zirconate titanate (PZT) material [2] and also other perovskites, forming a wide range of versatile crystalline solid solutions, such as $\text{Pb}(\text{Mg}_{1/3}\text{Nb}_{2/3})\text{O}_3\text{-PbTiO}_3$ or PMN-PT and $\text{Pb}(\text{Zn}_{1/3}\text{Nb}_{2/3})\text{O}_3\text{-PbTiO}_3$ or PZN-PT [2, 80]. These PT-based family members of ferroelectrics are widely used in multilayer capacitors, actuators, sensors, transducers, pyroelectric detectors and electro-optic devices.

During several past decades, many experiment [96-98] studies were carried out on various phase transformation and crystal structures of lead-based solid solutions consisting of normal and relaxor perovskite ferroelectrics. These compounds have attracted a growing fundamental and practical interest because of their excellent dielectric, piezoelectric and electrostriction properties which are useful in actuating

and sensing applications [95, 99]. Experimentally it has been reported that a variety of complex-mixed perovskite ferroelectrics with a complex occupation of the *A* and/or *B* site in the crystal lattice and exhibiting the diffuse phase transition behavior have a nanometer scale heterogeneity in composition [100-101]. In the 1950s, Smolenski and coworkers [85-86] investigated many cation substitutions into PbTiO_3 in a search for a new ferroelectric material. In this kind of substitution, the general guidelines are that the ionic sizes should be comparable to those of Ti^{4+} ion and the combination must yield the same average charge as Ti^{4+} to maintain charge neutrality. Many such compositions take on the complex perovskite structure, and their properties have been extensively reported by several researchers [102-104].

Lead magnesium niobate (PMN) is nowadays acknowledged as the representative of relaxor ferroelectrics [84]. The real macroscopic phase transition of the first order to rhombohedral long-range ferroelectric ordered phase has been detected in PMN at about 200 K by cooling in an external dc electric field [102]. Though the Curie temperature or better yet, Curie range of PMN is well below room temperature where it can be easily shifted upward with PT additions, a normal or ordered ferroelectric compound which has a transition at 490 °C. A spontaneous (zero field) phase transition was indicated in the solid solution PMN-PT as a result of a change in the degree of ordering induced by substitution of cationic sites. An addition of ~28% PT causes the material to revert to a normal ferroelectric tetragonal phase with $T_C \sim 130$ °C [103].

The $(1-x)\text{PMN}-(x)\text{PT}$ system also shows a morphotropic phase boundary (MPB) near $x \sim 0.34$, separating pseudo-cubic phase and tetragonal phases (Figure 2.27) [103]. As observed in other systems such as $(1-x)\text{PZN}:(x)\text{PT}$ and $(1-x)\text{PZ}:(x)\text{PT}$

or PZT, anomalously large dielectric and piezoelectric properties are observed for compositions lying near the MPB. The piezoelectric properties of PMN-PT system, however, are much higher compared with PZT system.

There is a considerable interest in PMN-PT ceramics due to their high strains with low hysteresis losses. These compounds also exhibit a broad maximum in the dielectric constant, and the temperature of the dielectric maximum also increases with the testing frequency as shown in Figure 2.28. These properties make the materials particularly suitable for use in electrostrictive actuator, sensor and piezoelectric devices.

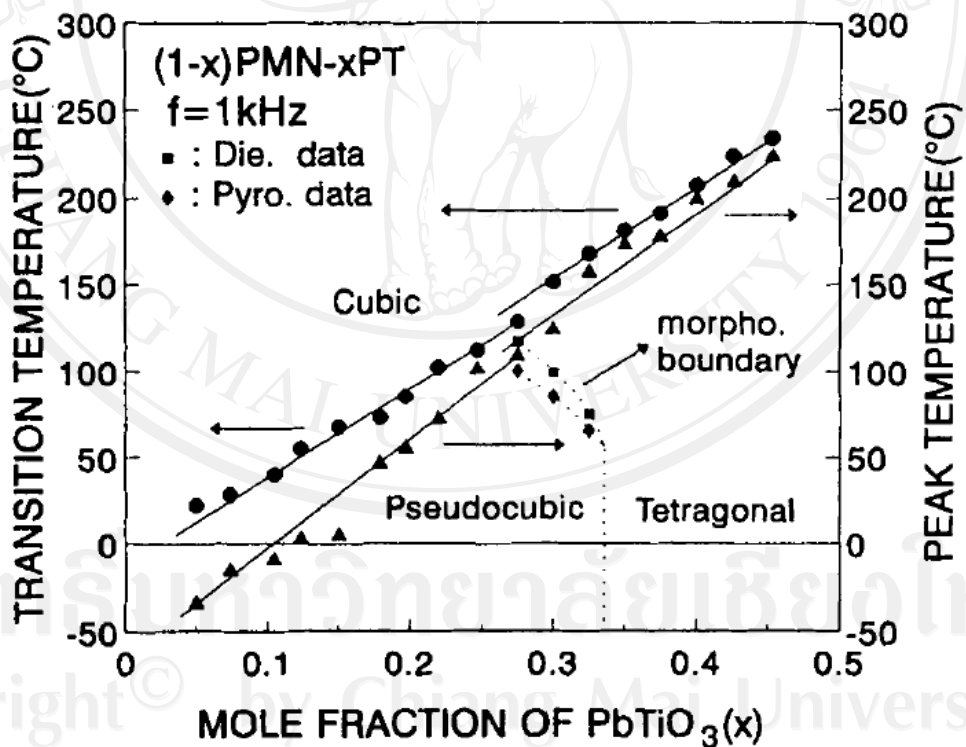


Figure 2.27 Phase diagram of the solid-solution of the PMN-PT system showing the morphotropic phase boundary (solid circles = calculated data and open circles = experimental data) [103]

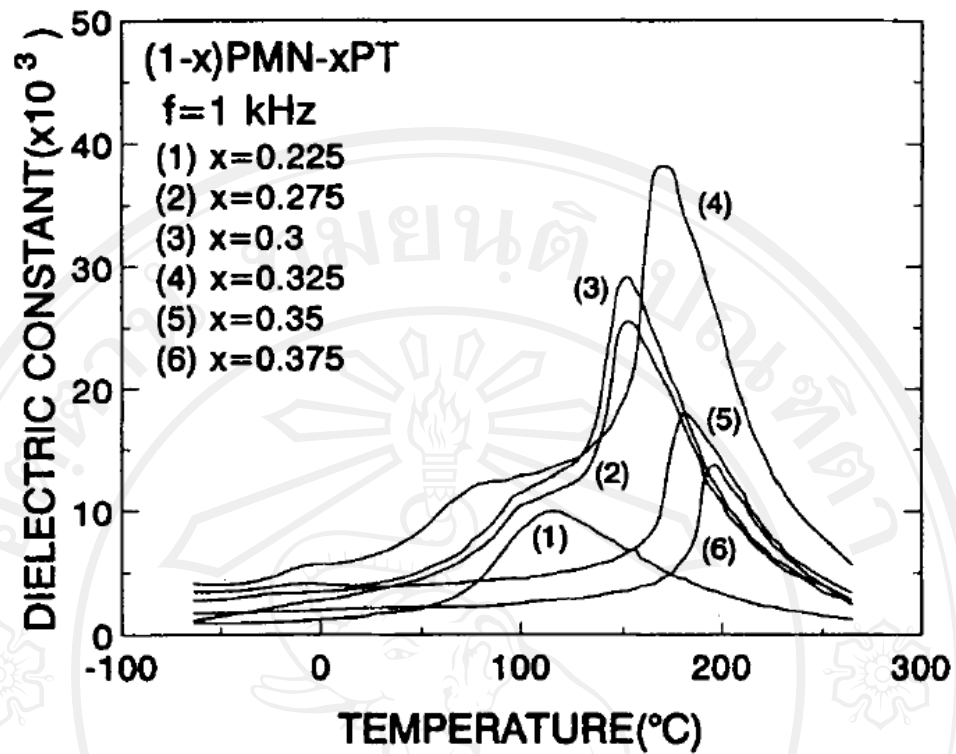


Figure 2.28 Dielectric behavior of (1-x)PMN-xPT ceramics (at 1 kHz) as a function of temperature [103].

Table 2.1 Dielectric and piezoelectric properties of (1-x) PMN: x PT [104]

Sample <i>x</i>	ϵ_r	$\tan \delta$	Unpoled				Poled					
			$\epsilon_{r, \max}$	T_C (°C)	$\tan \delta_{\max}$	d_{33}	ϵ_r	$\tan \delta$	$\epsilon_{r, \max}$	T_C (°C)	$\tan \delta_{\max}$	d_{33}
0.225	3533	0.032	29552	112	0.036	297	1695	0.022	28688	114	0.042	96
0.25	2778	0.031	30192	127	0.061	305	2435	0.018	28714	130	0.072	124
0.275	2873	0.035	33432	136	0.045	353	2091	0.030	31986	138	0.051	130
0.3	3782	0.034	36469	139	0.035	669	4936	0.027	33289	143	0.057	136
0.325	4170	0.029	33350	155	0.029	663	5260	0.018	30048	159	0.049	156
0.35	3190	0.013	30623	177	0.098	456	3119	0.006	29020	182	0.069	230
0.375	2434	0.015	28524	190	0.018	405	2781	0.011	28126	198	0.038	191
0.4	2097	0.016	27156	202	0.030	323	2371	0.010	25189	207	0.044	204

All rights reserved

2.10 Lead zirconate titanate-lead zinc niobate

[(Pb(Zr_{1/2}Ti_{1/2})O₃–Pb(Zn_{1/3}Nb_{2/3})O₃ or PZT-PZN)] systems

The piezoelectric solid solution lead zirconate titanate [Pb(Zr_{1-x}Ti_x)O₃ (PZT)] was found to host exceptionally high dielectric and piezoelectric properties for compositions close to the morphotropic phase boundary (MPB) [30]. This MPB is located around PbTiO₃:PbZrO₃ ~ 1:1 and separates the Ti-rich tetragonal phase from the Zr-rich rhombohedral phase [105]. Most commercial PZT ceramics are thus designed in the vicinity of the MPB with various dopings in order to achieve high properties.

Lead zinc niobate [Pb(Zn_{1/3}Nb_{2/3})O₃ (PZN)] is an important relaxor ferroelectric material with the rhombohedral structure at room temperature. A diffuse phase transition from the paraelectric state to a ferroelectric polar state occurs at 140 °C [106]. Extensive research has been carried on PZN single crystals because of their excellent dielectric, electrostrictive, and optical properties [107].

In addition, PZN has a low tolerance factor and small electronegativity difference between the cations and the pyrochlore phase appears to be more thermodynamically stable than the perovskite phase [108]. Hot isostatic pressing was reported to be able to produce phase-pure perovskite PZN ceramics [109]. However, relatively poor piezoelectric properties were measured in the as-pressed ceramic. Various chemical additives, such as Ba(Zn_{1/3}Nb_{2/3})O₃, BaTiO₃, and SrTiO₃ have thus been explored in an attempt to stabilize the perovskite PZN ceramic and retain the excellent piezoelectric properties.

Since both PZT and PZN have perovskite structure and are known to have excellent dielectric and piezoelectric properties, it is suggested to alloy PZN with PZT

to stabilize and optimize the PZN ceramics. So, recently, there have been lots of studies in lead zirconate titanate-lead zinc niobate [$(\text{Pb}(\text{Zr}_{1/2}\text{Ti}_{1/2})\text{O}_3\text{-Pb}(\text{Zn}_{1/3}\text{Nb}_{2/3})\text{O}_3$ or PZT-PZN)] systems [110-113].

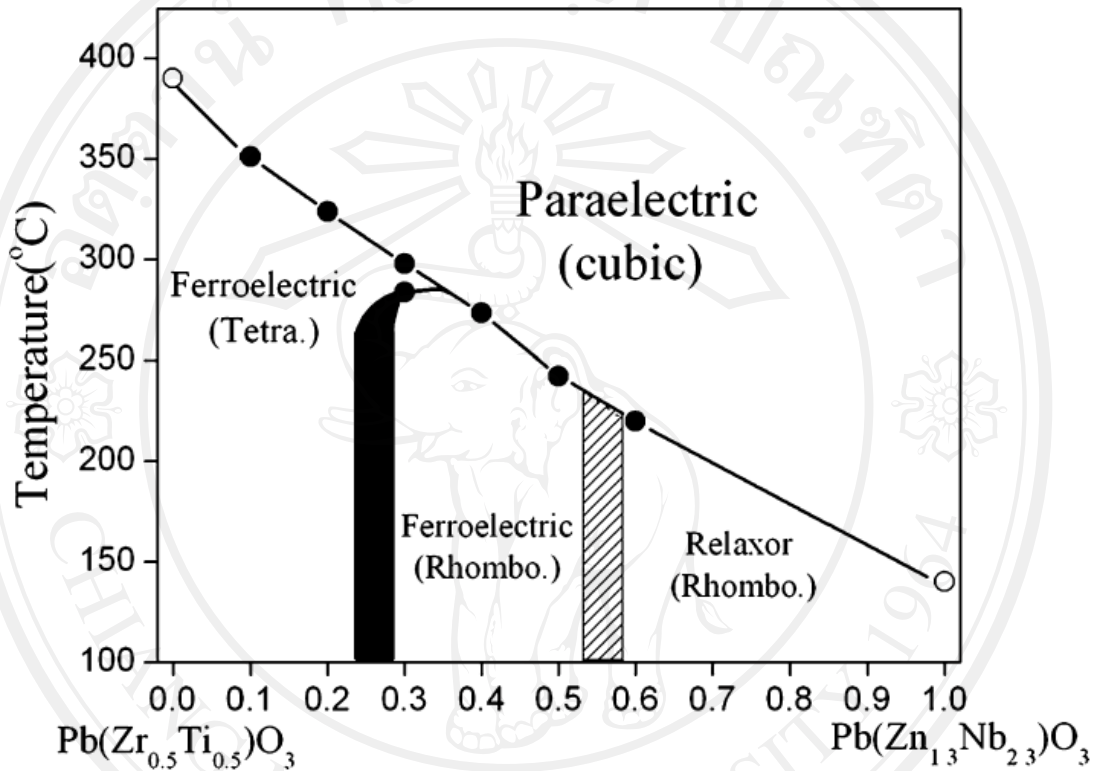


Figure 2.29 The proposed phase diagram for the $\text{Pb}(\text{Zn}_{1/3}\text{Nb}_{2/3})\text{O}_3\text{-Pb}(\text{Zr}_{1/2}\text{Ti}_{1/2})\text{O}_3$ pseudo binary solid solution system [113]

One of previous studies [114] revealed the investigation of crystal structure change as a function of composition in $(1-x)\text{PZT}\text{-}(x)\text{PZN}$ ceramic systems where $x = 0.1, 0.2, 0.3, 0.4,$ and 0.5 . The results suggested that the morphotropic phase boundary (MPB) is located between $x = 0.2$ and 0.3 according to observations made on ceramics prepared with the columbite method. When $x \leq 0.2$, the tetragonal phase dominates at

ambient temperatures, while in the range of $x \geq 0.3$, the rhombohedral phase dominates.

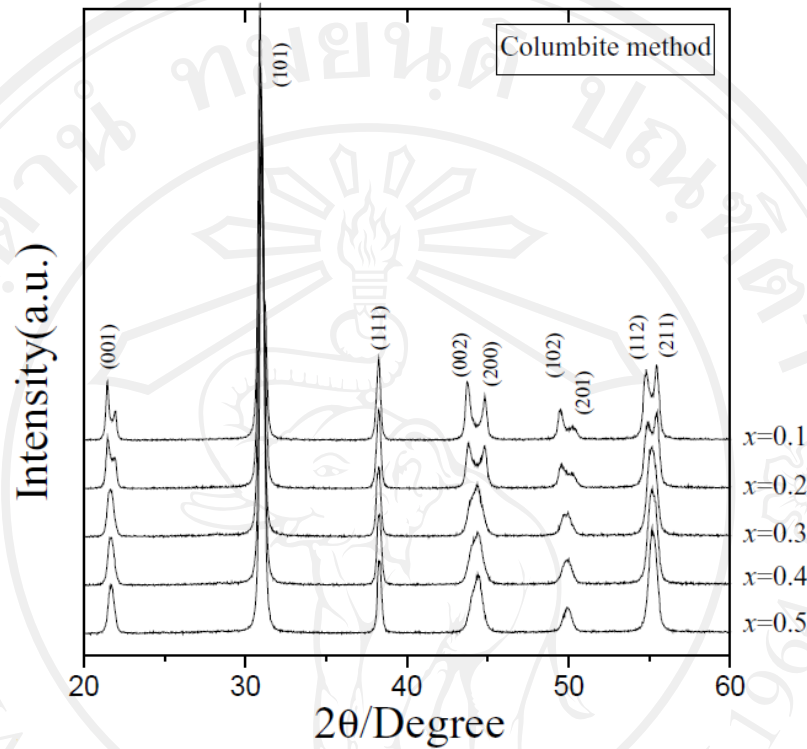


Figure 2.30 The XRD patterns of $x\text{PZN}-(1-x)\text{PZT}$ ceramics sintered at 1200 °C for 2 hours to illustrate the change in crystal structure as a function of composition for columbite method [114]

2.11 Literature Reviews

In 1998, Acharyya [60] studied the nonequilibrium phase transition in the kinetic Ising model. The non-equilibrium dynamic phase transition, in the kinetic Ising model in presence of an oscillating magnetic field, has been studied both by Monte Carlo simulation (in two dimensions) and by solving the mean-field dynamical equation of motion for the average magnetization. The temperature variations of hysteretic loss (loop area) and the dynamic correlation have been studied near the

transition point. The transition point has been identified as the minimum-correlation point. The hysteretic loss becomes maximum above the transition point. An analytical formulation has been developed to analyze the simulation results. A general relationship among hysteresis loop area, dynamic order parameter, and dynamic correlation has also been developed.

In 1999, Chakrabarti *et al.* [56] reviewed the dynamic hysteresis and transitions in ferromagnets via both aspects of theoretical and experimental studies. It can be concluded that when an interacting many-body system, such as a magnet, is driven in time by an external perturbation, such as a magnetic field, the system cannot respond instantaneously due to relaxation delay. The response of such a system under a time-dependent field leads to many novel physical phenomena with intriguing physics and important technological applications. For oscillating fields, one obtains hysteresis that would not occur under quasistatic conditions in the presence of thermal fluctuations. Under some extreme conditions of the driving field, one can also obtain a nonzero average value of the variable undergoing such “dynamic hysteresis”. This nonzero value indicates a breaking of the symmetry of the hysteresis loop about the origin. Such a transition to the “spontaneously broken symmetric phase” occurs dynamically when the driving frequency of the field increases beyond its threshold value, which depends on the field amplitude and the temperature. Typically, at fixed temperature T and field amplitude h_0 , the dynamic hysteresis loss A increases with increasing frequency ω for low values of ω . This is because, for low values of ω , the effective delay in the response increases as ω increases. In general, for a fixed ω , A increases with decreasing T and increasing h_0 until A saturates. Eventually, as the driving frequency exceeds a threshold value (dependent on h_0 and T), the loop area A

starts decreasing, because of the increase in the effective delay. The observed variation of the loop area A with frequency ω can be fitted to a form of $A = A_0 + h_0^\alpha \omega^\beta g\left(\frac{\omega}{h_0^\gamma}\right)$, with the scaling exponents α , β , and γ and with the scaling function g having a suitable nonmonotonic form such that $g(x) \rightarrow 0$ as $x \rightarrow 0$ or ∞ . A_0 is the loop area in the zero frequency limit. Similar dynamic transitions also occur for pulsed and stochastically varying fields.

The same year, Liu *et al.* [115] investigated the frequency response and scaling of hysteresis for ferroelectric $\text{Pb}(\text{Zr}_{0.52}\text{Ti}_{0.48})\text{O}_3$ thin films deposited by laser ablation. The ferroelectric hysteresis response against periodically varying electric field over frequency range of 10^{-2} - 10^5 Hz and amplitude range of 2-45 kV/cm for $\text{YBa}_2\text{Cu}_3\text{O}_7$ (YBCO)/ $\text{Pb}(\text{Ti}_{0.48}\text{Zr}_{0.52})\text{O}_3$ (PZT)/YBCO thin film capacitors prepared by laser ablation is measured by utilizing the Sawyer-Tower circuit. Given amplitude Δ of the field, the hysteresis area $\langle A \rangle$ first grows and then decays as a function of frequency ϕ . At low and high ranges of frequency, $\langle A \rangle$ can be scaled as $\langle A \rangle \propto \phi^{1/3} \Delta^{2/3}$ and $\langle A \rangle \propto \phi^{-1/3} \Delta$, respectively. It is established that the dynamic hysteresis at the high frequency range for a PZT thin film capacitor does not follow the theoretically predicted scaling law. An empirical scaling law $\langle A \rangle \propto \phi^{1/3} (\Delta - \Delta_0)^{2/3} / (1 + b \phi^{2/3} \Delta^{-1/3})$ with Δ_0 the critical field and b a constant, is proposed to characterize the frequency and amplitude dependence of the hysteresis area over all the frequency range. In addition, the remnant polarization P_r and coercive field E_C as function of ϕ are investigated, respectively, revealing a single-peaked pattern of both P_r and E_C .

In 2003, Park *et al.* [12] studied the scaling behavior of ferroelectric hysteresis loop in pulsed-laser-deposited $\text{SrBi}_2\text{Ta}_2\text{O}_9$ thin film grown on a highly oriented Pt/Ti/SiO₂/Si substrates using pulsed laser ablation. The hysteresis loop of ferroelectric $\text{SrBi}_2\text{Ta}_2\text{O}_9$ was studied as a function of applied field amplitude. A scaling analysis of ferroelectric hysteresis loop area showed $A \propto E^\alpha$. The value of scaling exponent, $\alpha = 0.40$, is not similar to the reported theoretical and experimental values. This result shows the possibility that both ferroelectric bulk and thin-film systems may have different universal behaviors. Influence of potential in the surface of $\text{SrBi}_2\text{Ta}_2\text{O}_9$ thin film was measured in the dc applied field range from 0 to 8 V by using electro force microscopy. Roughness of surface potential of $\text{SrBi}_2\text{Ta}_2\text{O}_9$ thin film changed rapidly around the coercive voltage, $V_C \sim 1.5$ V. It is believed that the switching effect of $\text{SrBi}_2\text{Ta}_2\text{O}_9$ thin film includes surface polarization at the surface of the thin film as well as pure spontaneous polarization in the bulk.

In 2005, Liu *et al.* [116] determined the dynamic scaling of hysteresis dispersion in three representative ferroelectric $\text{Pb}(\text{Ti}_{0.48}\text{Zr}_{0.52})\text{O}_3$ (PZT), $\text{Bi}_2\text{Sr}_2\text{Ta}_5\text{O}_9$ (SBT) and $\text{Bi}_4\text{Ti}_3\text{O}_{12}$ (BTO) thin films and one 1-3 $\text{Pb}_{0.95}\text{La}_{0.05}\text{TiO}_3$ (PLT)/polymer composites, measured using the Sawyer–Tower (ST) method, focusing on the dependence of the hysteresis area as a function of the amplitude E_0 and frequency f of the external electric field E . It is found that the one-parameter scaling of the single-peaked hysteresis dispersion applies to the three types of ferroelectric thin films and a Ginzburg–Landau (GL) model system where the domain reversal can be kinetically described by a unique characteristic time. It is confirmed by all of the three ferroelectric systems that the effective characteristic time for the domain reversal is

inversely proportional to the field amplitude, while this scaling does not work for the composite system.

In 2006, Yimnirun *et al.* [16] observed the scaling behavior of dynamic hysteresis in commercial soft lead zirconate titanate bulk ceramics (PKI-552, Piezo Kinetics Inc., USA). The results showed that the scaling relation of hysteresis area $\langle A \rangle$ against frequency f and field amplitude E_0 for the saturated loops of the soft lead zirconate titanate bulk ceramic takes the form of $\langle A \rangle \propto f^{-1/4} E_0$, which differs significantly from that of the theoretical prediction and that of the thin film. This indicates that the scaling relation is dimension dependent and that depolarizing effects in the interior must be taken into account to model bulk materials. Additionally, the scaling relation for the minor loops takes the form of $\langle A \rangle \propto f^{-1/3} E_0^3$, which is identical to that of the thin film as both cases contain similar 180° domain-reversal mechanism. Later in 2007, they also observed the dynamic hysteresis and scaling behavior of commercial hard lead zirconate titanate bulk ceramics (APC-840, APC International, Ltd., USA) [17]. The scaling relation of ferroelectric hysteresis area $\langle A \rangle$ against frequency f and field amplitude E_0 for the saturated loops of the hard lead zirconate titanate bulk ceramic takes the form of $\langle A \rangle \propto f^{-0.28} E_0^{0.89}$, while that for the minor loops takes the form of $\langle A \rangle \propto f^{-0.43} E_0^{3.19}$. In both cases, the scaling relations are similar to those of its soft counterpart. This indicates that the dynamic behaviors and scaling relations in bulk ceramics are mainly governed by the domain states and structures, while the distinct types of complex defects contribute mainly to the difference in the coercive field observed in hard and soft ceramics.

In 2008, Bhattacharyya *et al.* [22] investigated the scaling behavior of dynamic hysteresis of deformed helix ferroelectric liquid crystals (DHFLCs). The

hysteresis areas $\langle A \rangle$ for the saturated loops of a deformed helix ferroelectric liquid crystal, viz., (S)-4-(2-methyloctanoyl) 4'-biphenyl-4-octyloxybenzoate (MIP0806) have been studied. The scaling laws $\langle A \rangle \propto f^{0.24} E_0^{0.68}$ and $\langle A \rangle \propto f^{0.28} E_0^{0.70}$ connecting frequency (f) and amplitude (E_0) of the applied signal are found to be valid close to and far away from the SmA-SmC* transition temperature (104 °C), respectively. The formation of ferroelectric monodomain in MIP0806 is weakly constrained by surface and dipolar interactions, which might be responsible for the observed small deviation obtained from theoretically predicted scaling laws.

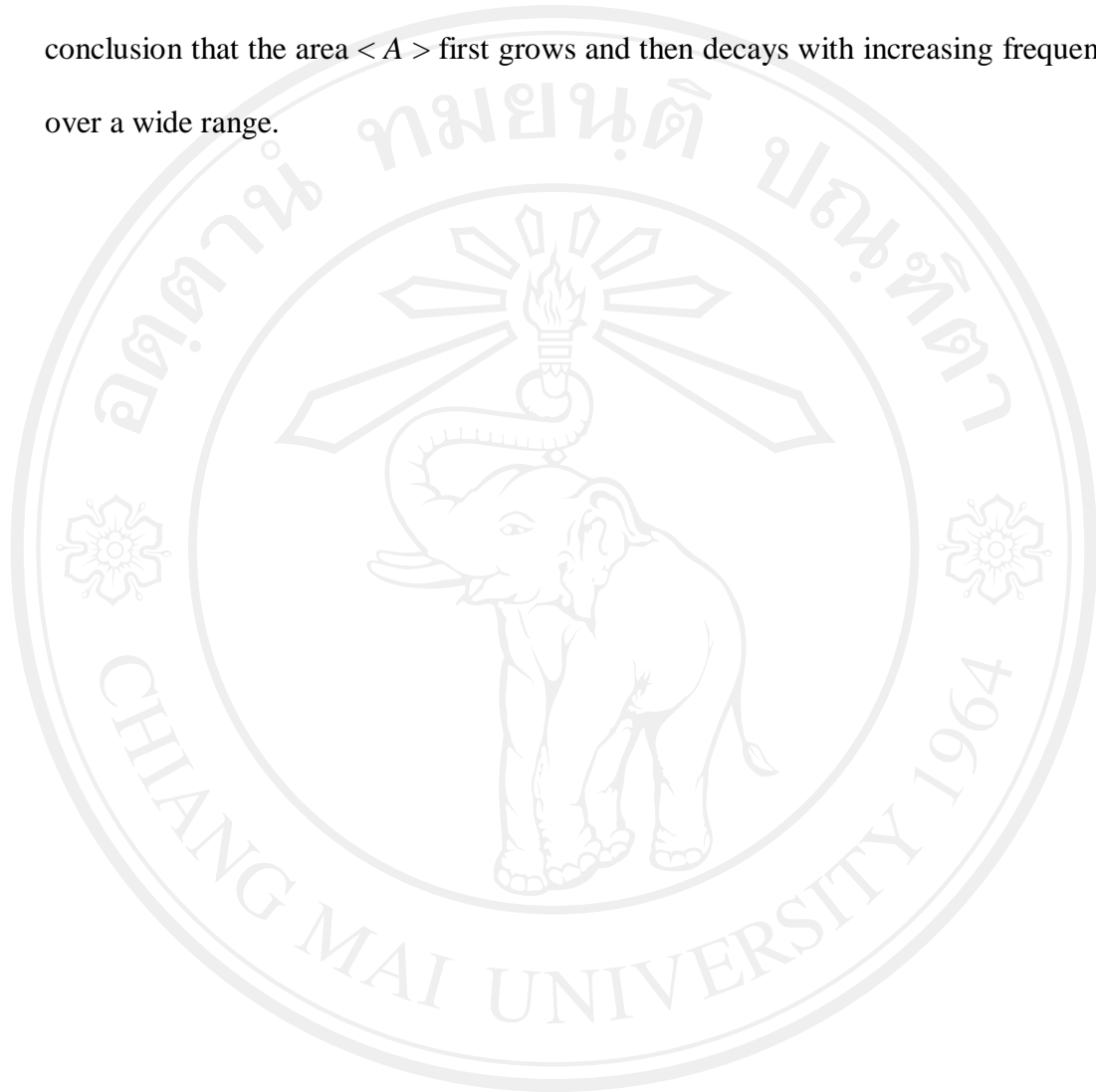
In addition, Yang *et al.* [21] have studied the evolution of electric field amplitude dependent scaling behaviors in ferroelectric films over a broad temperature range of 0.5 mol% Mn doped $\text{Pb}_{0.5}\text{Sr}_{0.5}\text{TiO}_3$ (PSMT05) and $0.7\text{Pb}(\text{Mg}_{1/3}\text{Nb}_{2/3})\text{O}_3$ – 0.3PbTiO_3 (0.7PMN-0.3PT) films. The evolution of the electric field amplitude (V_0) dependent scaling of dynamic hysteresis area ($A \propto V_0^\alpha$) with temperature in Mn doped (Pb,Sr)TiO₃ film was analyzed. α exhibited different values under three temperature regions: (I) when $T < T_C$, namely, the ferroelectric state, $\alpha = 2/3$. The scaling of the dynamic hysteresis in this region represents the kinetic picture of intrinsic ferroelectric domain nucleation, growth, and reversal. (II) From T_C to 520 K, α increases approaching to 2. Here the ferroelectric domain has been replaced by PNRs distributing in the paraelectric matrix. In addition, the effect of mobile defects (e.g., oxygen vacancy) begins to occur and becomes more prominent with the increase in temperature. Therefore, the competition between the PNRs and mobile defects may be another cause for the enhancement in the value of α . (III) Above 520 K, ionized oxygen vacancies are dominative, which can move a long distance under the applied electric field, the scaling behavior shows quadratic ($\alpha = 2$) power-law due to Joule

loss in the process of oxygen vacancies' movement. The evolution of the scaling behavior in 0.7PMN-0.3PT films was also checked and it revealed similar results of α . This study suggests a quantitative criterion to distinguish the intrinsic ferroelectric hysteresis from artificial one.

In 2009, Chen *et al.* [117] observed the scaling behaviors of dynamic hysteresis in Zr-rich lead zirconate titanate bulk ceramics. The PZT 95/5 ceramics prepared by the conventional solid-state reaction were investigated hysteresis behaviors and their scaling relations under two ferroelectric phases, a high-temperature rhombohedral phase ($F_{R(HT)}$) and a low-temperature rhombohedral phase ($F_{R(LT)}$). The scaling relations of the saturated hysteresis loops for PZT 95/5 ceramics take the forms $\langle A \rangle \propto f^{0.16} E_0$ and $\langle A \rangle \propto f^{-0.01} E_0^{0.2}$ for low f and high f at fixed temperature, respectively. The forms are different from the theoretical predictions and other experimental results but are the same for $F_{R(LT)}$ and $F_{R(HT)}$, which implies that the compositions and crystal structures can influence the scaling laws while the different space groups in rhombohedral phase cannot.

In 2010, Yu *et al.* [118] examined the dynamic ferroelectric hysteresis scaling behavior of 40BiScO₃-60PbTiO₃ bulk ceramics. (1- x)BiScO₃- x PbTiO₃ (BSPT) ceramics are the promising candidates for relatively high temperature sensor use and actuator applications. Polarization-field (P - E) hysteresis loops of 40BiScO₃-60PbTiO₃ bulk ceramics were measured under sinusoidal electric fields over a frequency range of 10⁻²-10² Hz and an amplitude range of 20-50 kV/cm. The scaling relations of the hysteresis loop area $\langle A \rangle$ versus the frequency f and amplitude E_0 of the applied field for the saturated loops take different forms in the low (0.01 Hz $< f < 1$ Hz) and high (1 Hz $< f < 100$ Hz) frequency ranges. For low f range, the scaling relation takes the

form of $\langle A \rangle \propto f^{0.05} E_0^{0.6}$, and takes the form of $\langle A \rangle \propto f^{-0.01} E_0^{0.3}$ for high f range. Combining the information from these two relations, one can draw the conclusion that the area $\langle A \rangle$ first grows and then decays with increasing frequency f over a wide range.



ลิขสิทธิ์มหาวิทยาลัยเชียงใหม่
Copyright© by Chiang Mai University
All rights reserved